Novel Vortex Approach for Downwash and Outwash of a Tandem rotor in Ground Effect

Jian Feng Tan[1] and Yi Ming Sun.[2]
School of Mechanical and Power Engineering, Nanjing Tech University, Nanjing, 211816, P.R. China

George N. Barakos[3]
CFD Laboratory, School of Engineering, University of Glasgow, Glasgow G12 8QQ, UK

A vortex-based approach is employed to predict downwash and outwash of a tandem rotor in ground effect and provide an understanding of its wake. The aerodynamic loads of the blades are represented through a panel method, and the behavior of the wake is captured by a viscous vortex particle method. The viscous effects of the ground are accounted for by a viscous boundary model satisfying the no-slip and non-penetration boundary conditions. The method is first validated for an isolated full-scale Lynx tail rotor and a 172 mm-diameter scale rotor in ground effect. The results show that the predicted trajectories of the tip vortices and the radial velocity profiles compare favorably with experiments and published CFD results. Results for a model CH-47D are then compared with experiments for the downwash and outwash of the tandem rotor. As opposed to the isolated single rotor, a radial outward expansion in the overlapping area is observed, and the peak and the corresponding vertical distance of the velocity maximum of the radial outwash flow for the tandem rotor is larger. Moreover, the rotational direction of the tandem rotor leads to a wake with several vortical interactions resulting in different outwash on the port and starboard sides.

Nomenclature

b, f = edge lengths of the rectangular panel, m

h_{xi}, h_{yi}, h_{zi} = edge lengths of the integration cuboid, m

[1] Lecturer, School of Mechanical and Power Engineering, Nanjing Tech University, Nanjing, People's Republic of China; JianfengTan@njtech.edu.cn.
[2] Graduate, School of Mechanical and Power Engineering, Nanjing Tech University, Nanjing, People's Republic of China; yimingsun2016@163.com.
[3] Professor, School of Engineering, University of Glasgow, Glasgow, UK; George.Barakos@glasgow.ac.uk.

K = smoothing function, non-dimensional

K_ε = Biot-Savart kernel, non-dimensional

G = free-space Green's function, non-dimensional

$\boldsymbol{n}$ = outward unit normal vector of surface, non-dimensional

p = local pressure, Pa

p^{for} = local pressure of the forward rotor, Pa

p^{aft} = local pressure of the aft rotor, Pa

p_{ref} = far-field reference pressure, Pa

$\boldsymbol{r}$ = position vector, m

s = tangential direction of the surface panel, non-dimensional

$S_{\text{multi-r}}$ = multi-rotor blade surface, m^2

$S_{\text{multi-rw}}$ = multi-rotor wake surface, m^2

t = time, s

$\mathbf{t}$ = tangential of the body boundary, non-dimensional

$\boldsymbol{u}$ = fluid velocity, m/s

$\mathbf{u}_\infty$ = free-stream velocity, m/s

$\mathbf{u}_{\text{slip}}$ = induced velocity due to vorticity, m/s

$\boldsymbol{v}$ = local fluid velocity near blades, m/s

$\boldsymbol{v}_{\text{multi-r}}$ = velocity of a point on the multi-rotor surface, m/s

$\boldsymbol{v}^{\text{for}}$ = local fluid velocity of the forward rotor, m/s

$\boldsymbol{v}^{\text{for}}_{\text{ref}}$ = referenced velocity of the forward rotor, m/s

$\boldsymbol{v}^{\text{aft}}$ = local fluid velocity of the aft rotor, m/s

$\boldsymbol{v}^{\text{aft}}_{\text{ref}}$ = referenced velocity of the aft rotor, m/s

$\boldsymbol{v}^{\text{for}}_{\text{w}}$ = convection velocity of the tip vortex of the forward rotor, m/s

$\boldsymbol{v}^{\text{aft}}_{\text{w}}$ = convection velocity of the tip vortex of the aft rotor, m/s

$\boldsymbol{v}^{\text{for}}_{\text{ind}}$ = induced velocity of the forward rotor wake, m/s

$\boldsymbol{v}_{\text{ind}}^{\text{aft}}$ = induced velocity of the aft rotor wake, m/s

$\boldsymbol{x}_j$ = position of a particle, m

$\boldsymbol{x}_{\text{for}}$ = blade position of the forward rotor, m

$\boldsymbol{x}'_{\text{for}}$ = tip vortex position of the forward rotor, m

$\boldsymbol{x}_{\text{aft}}$ = blade position of the aft rotor, m

$\boldsymbol{x}'_{\text{aft}}$ = tip vortex position of the aft rotor, m

$\boldsymbol{\alpha}_j$ = vector-valued vorticity of a particle, 1/s

$\boldsymbol{\gamma}$ = bound circulation of vortex sheet, 1/s

ζ_ε = kernel function, non-dimensional

μ = doublet of multi-rotor blades, m^4/s

v = kinematic viscosity, m^2/s

ρ = air density, kg/m^3

σ = source of multi-rotor blades, m^3/s

ϕ = velocity potential, m^2/s

$\phi_{\text{b}}^{\text{for}}$ = velocity potential induced by the forward rotor blades, m^2/s

$\phi_{\text{w}}^{\text{for}}$ = velocity potential induced by the forward rotor wake, m^2/s

$\phi_{\text{b}}^{\text{aft}}$ = velocity potential induced by the aft rotor blades, m^2/s

$\phi_{\text{w}}^{\text{aft}}$ = velocity potential induced by the aft rotor wake, m^2/s

ψ = stream function, m^2/s

$\boldsymbol{\omega}$ = vorticity of flow field, 1/s

$\Omega_i(t)$ = bodies, non-dimensional

ΔF_k = aerodynamic load on the panel, N

ΔS_{k} = panel area, m^2

DWOW = downwash and outwash

IGE = in ground effect

OGE = out of ground effect

I.Introduction

Helicopters operating in ground effect (IGE) have so far been widely investigated. Nevertheless, there are still issues related to the downwash and outwash of rotors that need investigating [1-3]. Contrary to a rotor operating out of ground effect (OGE), the presence of the ground significantly alters the rotor aerodynamics and generates more complex and unsteady flow field. Also, since the ground effect alters the induced velocity in the plane of the rotor, the performance of the rotorcraft is enhanced. This effect has been documented and observed since the dawn of the helicopter age. Furthermore, the induced velocity near the ground may be large enough to produce a wall jet and lift up loose surface items, such as dirt and sand, resulting in a phenomenon known as “brownout” [4-8]. This is a result of the interaction between the rotor wake and the ground plane, which forces the rotor slipstream to expand radially away from the rotor as it approaches the ground surface. In Ref.7, Phillips et al stated that the brownout characteristics of rotorcraft are extremely sensitive to the vortices of the wake, so the geometry and dynamics of the individual vortical structures within the flow alter markedly the resultant structure of the dust cloud under brownout condition. Additionally, the fundamental understanding of the fluid dynamics of the rotor wake as it interacts with the ground is a prerequisite to understanding and mitigating brownout [1]. However, investigations are mainly focus on the evolution and formation of wake of an isolated single rotor system. Contrary to the isolated single rotors, the downwash and outwash (DWOW) of multi-rotor configurations, especially overlapping tandem rotor systems, in ground effect, are more complex. This is because, unlike a single rotor, the DWOW of multi-rotor configurations is not axisymmetric. The flow components away from the tandem rotor in the longitudinal and lateral directions are different. Moreover, the flow along the longitudinal axis is not simple [9-11]. Also, few experimental and numerical investigations have been produced on the topic in the last few years. Even applying high-fidelity CFD tools, such as Helios (HELIcopter Overset Simulations), to the DWOW problem is a challenge due to the computational cost, boundary conditions, turbulence modeling, flow unsteadiness, and the large number of rotor revolutions required to stabilize the flow field. In addition, high-fidelity simulations of the DWOW require further research [10]. Therefore, a critical step in understanding the flow field of the multi-rotor IGE is the development of methods able to accurately and efficiently analyze the evolution of the rotor wake and capture the tip vortices and the DWOW characteristics.

The ground effect can be accounted for using several models. Simple mirror-image (MI) methods in which a rotor and its image were replaced by simple sinks [12] or sources [13] were first employed, whereas the structure of

the wake was not taken into account in this approach. A similar approach with a vortex cylinder model to account for the effect of wake was also proposed [14, 15]. In this method, the number of blades and the slipstream contraction were neglected. A continuous, distorted helical vortex model was also proposed, and the ground-plane boundary condition was enforced using a mirror image of the wake [16]. While the evolution of the tip vortices near the ground plane and the interaction between the tip vortices and the ground plane were not accounted for in this approach. Then, a momentum-based mathematical model with experimental corrections, including a wall jet theory, and a ground effect correction factor, was described by Kiseilowski and Douglas [17]. The wake contraction was taken into account to quickly evaluate the performance of overlapping and non-overlapping rotor configurations [18, 19]. Nevertheless, the drawback of this approach was the limited availability of experimental data for the corrections necessary in the model. Following that, simulations of the ground effect were attempted with varying degrees of success using free-wake methods. The free wake methods coupling with the MI technique to satisfy the non-penetration wall condition were reported in Refs [6, 20-23]. Although the MI approach has good computational efficiency, it is less suited to non-planar or otherwise irregular surfaces. Therefore, a more flexible, vortex-singularity-based model, was developed for the ground effect [24]. Nevertheless, viscous effect, that might be present when the tip vortices interact with the ground, was not modelled, as was the case with the method of images. Additionally, even though the free-wake methods could track the wake for very long distances behind the rotor, they involved a certain degree of empiricism in determining the vortex core radius and roll-up age.

Based on the vorticity-velocity formulation of the Navier–Stokes equations, the vorticity transport model [25, 26] coupled with a blade element rotor model and uniform meshes for the wake, provided a good representation of the formation and the evolution of the tip vortices and the brownout. However, computations [25, 26] had been run with an inviscid ground plane and the MI approach. Following this, a Viscous Vortex Particle Method (VPM) [27] with a blade element rotor model, an image ground method, and the Brinkmann penalty technique [28] was developed to model the outwash of small-scale rotors, including CH-53E and XV-15. Nevertheless, that approach based on the MI was less suited for non-planar, irregular surfaces, such as obstacles.

More recently, Computational Fluid Dynamics (CFD) tools, such as the OVERFLOW 2 [4], HMB [29], OVERTURNS [30-32], and Helios [10], have been increasingly used to predict velocity profiles, wake trajectories, and flow visualizations, to understand phenomena like the brownout. Vortex-tracking grids (VTGs) and refined overset meshes were used to capture the evolution of the tip vortices near the ground with approximately 22 million

grid points [31, 32]. The Helios tool, coupled with adaptive mesh refinement (AMR) and overset grids (approximately 0.5 billion grid points) was used to simulate the outwash of an isolated single rotor in ground effect [10]. However, the unsteadiness of the tip vortices and the outwash predicted by the CFD are affected by several factors, such as excessive numerical dissipation, and lack of high-density grids, needed to capture the rotor wake. Another challenge for grid-based CFD methods is that the tip vortex needs to be preserved for significantly long periods of time to capture its interaction with the ground. Therefore, efficient DWOW predictions of multi-rotors, such as the tandem rotor, IGE are of interest to the helicopter computational community, and vortex methods are attractive because of high efficiency.

The purpose of this work is to develop a vortex-based method able to predict the DWOW of the tandem rotor system. In this method, the aerodynamics of multi-rotor is described through an unsteady panel method, and the unsteady behavior of the wake near the ground plane is modelled through the viscous vortex particle method [33]. The viscous effects of the ground plane are accounted for by a viscous boundary model satisfying both the no-slip and non-penetration boundary conditions. This is implemented by generating a vortex sheet on the ground surface and diffusing the vortex into the flow field. Following the method description, the trajectories of the tip vortices of the full-scale Lynx tail rotor, the velocity profiles of a 172 mm-diameter rotor, and the DWOW of an isolated single rotor, and the corresponding overlapping tandem rotor (scaled model of CH-47D) IGE are computed and compared with experimental data and published CFD results to demonstrate and prove the method. Additionally, the wake structure, flow visualization, downwash and radial outwash profiles of the overlapping tandem rotor IGE are compared with that of the single rotor.

II.Computational Method

A. Aerodynamic Model of Multi-rotor Aircraft

A multi-rotor aircraft has a distinct trailed wake with its own IGE characteristics. This is because the flow field, especially in the transition region where the flow runs from vertical to horizontal, is dominated by the wake of the rotor blades [10, 11]. Successful aerodynamic analysis of the multi-rotor aircraft IGE requires capabilities for modelling unsteady airloads and vortices. Following this, the aerodynamics of the multi-rotor aircraft is first represented by the unsteady panel method [33]. Based on this method, the velocity potential of the multi-rotor is

defined in a global reference frame (X, Y, Z) in Fig. 1, which shows the position of the forward and aft rotors with respect to the ground plane, as

$$\phi(x,y,z,t)=\frac{1}{4\pi}\int_{S_{\text{multi-r}}}\mu\boldsymbol{n}\cdot\nabla\left(\frac{1}{r}\right)dS-\frac{1}{4\pi}\int_{S_{\text{multi-r}}}\sigma\left(\frac{1}{r}\right)dS+\frac{1}{4\pi}\int_{S_{\text{multi-rw}}}\mu\boldsymbol{n}\cdot\nabla\left(\frac{1}{r}\right)dS \tag{1}$$

where σ and μ are the source and doublet distributions placed on the multi-rotor blades ($S_{\text{multi-r}}$) and on the wake surface ($S_{multi\text{-rw}}$). $\boldsymbol{n}$ denotes the outward unit normal vector of the surfaces, and $\boldsymbol{r}$ is the position vector (x, y, z).

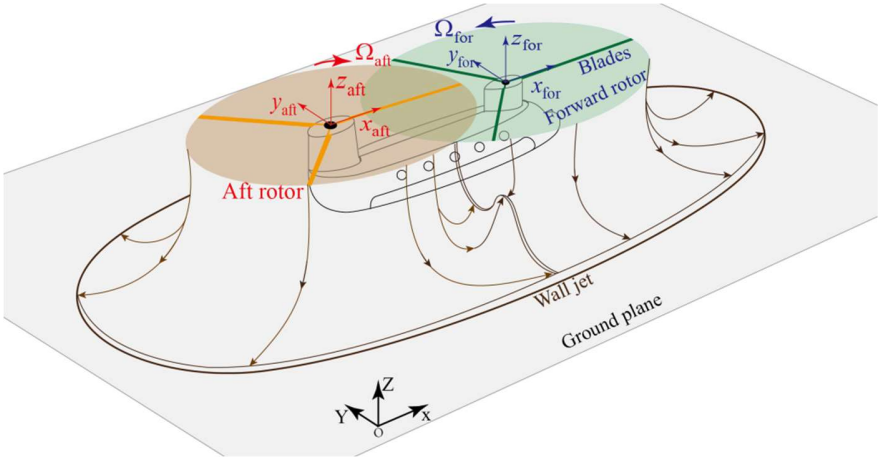

Fig. 1 Schematic of DWOW for a tandem rotor

The boundary conditions for the multi-rotor system require that the velocity component normal to the blades is zero. The boundary condition at infinity requires flow disturbances to decrease to zero. Both can then be expressed as:

$$\begin{cases}\dfrac{\partial\phi}{\partial n}-\boldsymbol{v}_{\text{multi-r}}\cdot\boldsymbol{n}=0 & \text{multi-rotor surface}\\ \lim\nabla\phi_{r\to\infty}=0 & \text{far-field boundary}\end{cases} \tag{2}$$

where $\boldsymbol{v}_{\text{multi-r}}$ is the velocity of a point on the multi-rotor surface $S_{\text{multi-r}}$.

The boundary condition at infinity is automatically fulfilled through Green's function. According to the Neumann boundary condition, and the trailing-edge Kutta condition, the surface boundary conditions are transformed to algebraic equations, and more details could be found in Ref. 33. And then the source and double distributions on all blades of the multi-rotor system are solved at the same time. The flow field of the multi-rotor is then determined and the unsteady pressure on the multi-rotor blade surfaces can be calculated using the velocity potential and the flow velocity through the Bernoulli's equation. Also, the interaction between the aft and forward

rotors which produces a complex flow field and unsteady airloads should be taken into account in the unsteady pressure.

$$\frac{\partial \phi}{\partial t}+\frac{1}{2}\boldsymbol{v}^2+\frac{1}{\rho}p=\frac{1}{\rho}p_{\mathrm{ref}} \tag{3}$$

The aft rotor wake impinges on the forward rotor blade surface resulting in a variation of the unsteady term $\partial\phi/\partial t$ of Eq.(3). The effect of the multi-rotor aerodynamic interaction is modelled thought the unsteady pressure term induced by the wake and the blades of both rotors. Thus, the non-dimensionalised form of the blade unsteady pressure is:

$$\begin{aligned} C_p^{\mathrm{for}} &= \frac{p^{\mathrm{for}}-p_{\mathrm{ref}}}{(1/2)\rho\left(\boldsymbol{v}_{\mathrm{ref}}^{\mathrm{for}}\right)^2}=1-\frac{\left(\boldsymbol{v}^{\mathrm{for}}\right)^2}{\left(\boldsymbol{v}_{\mathrm{ref}}^{\mathrm{for}}\right)^2}-\frac{2}{\left(\boldsymbol{v}_{\mathrm{ref}}^{\mathrm{for}}\right)^2}\left(\frac{\partial\phi_{\mathrm{b}}^{\mathrm{for}}}{\partial t}+\frac{\partial\phi_{\mathrm{w}}^{\mathrm{for}}}{\partial t}+\frac{\partial\phi_{\mathrm{b}}^{\mathrm{aft}}}{\partial t}+\frac{\partial\phi_{\mathrm{w}}^{\mathrm{aft}}}{\partial t}\right) \\ C_p^{\mathrm{aft}} &= \frac{p^{\mathrm{aft}}-p_{\mathrm{ref}}}{(1/2)\rho\left(\boldsymbol{v}_{\mathrm{ref}}^{\mathrm{aft}}\right)^2}=1-\frac{\left(\boldsymbol{v}^{\mathrm{aft}}\right)^2}{\left(\boldsymbol{v}_{\mathrm{ref}}^{\mathrm{aft}}\right)^2}-\frac{2}{\left(\boldsymbol{v}_{\mathrm{ref}}^{\mathrm{aft}}\right)^2}\left(\frac{\partial\phi_{\mathrm{b}}^{\mathrm{for}}}{\partial t}+\frac{\partial\phi_{\mathrm{w}}^{\mathrm{for}}}{\partial t}+\frac{\partial\phi_{\mathrm{b}}^{\mathrm{aft}}}{\partial t}+\frac{\partial\phi_{\mathrm{w}}^{\mathrm{aft}}}{\partial t}\right) \end{aligned} \tag{4}$$

where p_{ref} and ρ are the far-field reference pressure and air density. $\boldsymbol{v}^{\mathrm{for}}$, p^{for}, $\boldsymbol{v}_{\mathrm{ref}}^{\mathrm{for}}$ are the local fluid velocity, the local pressure, and the reference velocity, respectively, at each section of the forward rotor, while $\boldsymbol{v}^{\mathrm{aft}}$, p^{aft}, $\boldsymbol{v}_{\mathrm{ref}}^{\mathrm{aft}}$ are the local fluid velocity, the local pressure, and the reference velocity, respectively, at each section of the aft rotor. Also, $\phi_{\mathrm{b}}^{\mathrm{for}}$ and $\phi_{\mathrm{w}}^{\mathrm{for}}$ are the velocity potentials induced by the forward rotor blades and their wake, whereas $\phi_{\mathrm{b}}^{\mathrm{aft}}$ and $\phi_{\mathrm{w}}^{\mathrm{aft}}$ are the velocity potentials induced by the aft rotor blades and their wake.

The unsteady pressure term induced by both rotor blades can be directly described by the derivative of the velocity potential, whilst that of the tandem rotor wake can be transformed into the product of the induced velocity from the wake and the velocity of the wake, which is similar to the effect of tip-vortex filaments [34]. Those derivatives of the velocity potential can be expressed as:

$$\begin{aligned} \partial\phi_{\mathrm{b}}^{\mathrm{for}}/\partial t &= (\phi_{\mathrm{b}}^{\mathrm{for},t}-\phi_{\mathrm{b}}^{\mathrm{for},t-\Delta t})/\Delta t \\ \partial\phi_{\mathrm{b}}^{\mathrm{aft}}/\partial t &= (\phi_{\mathrm{b}}^{\mathrm{aft},t}-\phi_{\mathrm{b}}^{\mathrm{aft},t-\Delta t})/\Delta t \end{aligned} \tag{5}$$

$$\begin{aligned} \partial\phi_{\mathrm{w}}^{\mathrm{for}}/\partial t &= -\sum \boldsymbol{v}_{\mathrm{ind}}^{\mathrm{for}}(\boldsymbol{x}_{\mathrm{for}})\cdot\boldsymbol{v}_{\mathrm{w}}^{\mathrm{aft}}(\boldsymbol{x}'_{\mathrm{aft}}) \\ \partial\phi_{\mathrm{w}}^{\mathrm{aft}}/\partial t &= -\sum \boldsymbol{v}_{\mathrm{ind}}^{\mathrm{aft}}(\boldsymbol{x}_{\mathrm{aft}})\cdot\boldsymbol{v}_{\mathrm{w}}^{\mathrm{for}}(\boldsymbol{x}'_{\mathrm{for}}) \end{aligned} \tag{6}$$

where $\boldsymbol{x}_{\mathrm{for}}$, $\boldsymbol{v}_{\mathrm{w}}^{\mathrm{for}}$, $\boldsymbol{x}'_{\mathrm{for}}$ are blade position, velocity and position of the tip vortices of the forward rotor, and $\boldsymbol{x}_{\mathrm{aft}}$, $\boldsymbol{v}_{\mathrm{w}}^{\mathrm{aft}}$, $\boldsymbol{x}'_{\mathrm{aft}}$ are blade position, velocity and position of the tip vortices of the aft rotor, respectively. $\boldsymbol{v}_{\mathrm{ind}}^{\mathrm{for}}$ and $\boldsymbol{v}_{\mathrm{ind}}^{\mathrm{aft}}$ are the

velocity on the forward rotor induced by the aft rotor tip vortices, and the velocity on the aft rotor induced by the forward rotor tip vortices, respectively.

The aerodynamic forces on the panels of the multi-rotor system can then be computed as:

$$\Delta \boldsymbol{F}_k = -C_{pk}\left(\rho \boldsymbol{v}_{\mathrm{ref}}^2/2\right)_k \Delta S_k \boldsymbol{n}_k \tag{7}$$

where $\Delta \boldsymbol{F}_k$ is the aerodynamic load on the panel, ΔS_k is the panel area, and $\boldsymbol{n}_{\mathrm{k}}$ is its normal vector.

B. Wake Model of the Multi-rotor Aircraft

The interaction between the aft and forward rotors affects the geometry of the tip vortices and the vortex sheet which dominate the wake near the ground plane as shown in Fig. 1. The tip vortices emanating from the blade need to be preserved for significantly long periods of time to capture the interaction with the ground. So, the wake of the multi-rotor system is modelled here based on the viscous vortex particle method [33] which solves the Navier–Stokes equations in velocity-vorticity ($\boldsymbol{u}$, $\boldsymbol{\omega}$) in a Lagrangian frame of reference using vector-valued particles.

$$\frac{\partial \boldsymbol{\omega}}{\partial t} + \boldsymbol{u}\cdot\nabla\boldsymbol{\omega} = \nabla\boldsymbol{u}\cdot\boldsymbol{\omega} + \nu\nabla^2\boldsymbol{\omega} \tag{8}$$

where ν is kinematic viscosity, $\boldsymbol{\omega} = \nabla \times \mathbf{u}$ is the vorticity field associated with the velocity field.

The second term on the left hand-side describes the vortex particle convection which is solved using the fourth-order Runge-Kutta scheme, the Biot-Savart law, and symmetrical smoothing parameters. The right hand-side expresses the vortex stretching and viscous diffusion effects. The viscous diffusion effect $\nu\nabla^2\boldsymbol{\omega}$ is simulated through the Particle Strength Exchange (PSE) which suggests that the Laplacian operator ∇^2 can be replaced by an integral operator [35, 36]. The Laplacian operator in the viscous term can then be written as:

$$\nabla^2\boldsymbol{\omega} \approx \frac{2}{\varepsilon^2}\int_V \zeta_\varepsilon(\mathbf{x}-\mathbf{y})\left[\boldsymbol{\omega}(\mathbf{x})-\boldsymbol{\omega}(\mathbf{y})\right]d\mathbf{y} \tag{9}$$

where ζ_ε is a kernel function with Gaussian distribution, and ε is the smoothing radius.

The vortex stretching effect $\nabla\mathbf{u}\cdot\boldsymbol{\omega}$ is represented through a direct scheme which suggests that the velocity gradient can be expressed as a product of the kernel function gradient and the position gradient [37]. The particle velocity gradient in Eq. (8) can be written as follows:

$$\nabla \mathbf{u}(\mathbf{x},t) = -\sum_{j=1}^{N} \nabla\left[K_{\varepsilon}(\mathbf{x},\mathbf{x}_j)(\mathbf{x}-\mathbf{x}_j) \right] \times \boldsymbol{\alpha}_j$$

(10)

where K_ε is the Biot-Savart kernel for the velocity evaluation. $\boldsymbol{x}_j$ and $\boldsymbol{\alpha}_j$ are the rotor position and the vector-valued vorticity, respectively.

The operation count of this method is reduced through the Fast Multipole Method (FMM) [38]. The vortices are shed from the blade surfaces via the applied Neumann boundary condition and by converting shed-wake doublet panel to vorticity [33], transported based on the Eq.(8).

C. Viscous Model of the Ground Plane

Dealing with boundaries on the ground or obstacles in methods like the free-wake method, the vorticity transport model, or the vortex particle method, may be difficult. This is because formulating the boundary condition on a solid wall is notoriously problematic. The difficulty arises by the absence of a vorticity boundary condition for the Navier–Stokes equations, equivalent to no-slip at the wall. A viscous boundary model, which is suitable for different geometries, such as the ground plane and obstacles, is proposed by considering the no-slip boundary condition and the non-penetration boundary condition based on a vorticity sheet concept [39-41].

When a set of bodies, such as the ground and obstacles, indicated as $\Omega_i(t)$, i.e. ¡ $^3 \setminus \cup\{\Omega_i(t)\}$ is immersed in a flow, its effect can be summarized in two expressions of the boundary conditions: the flow cannot go through the solid wall, which is interpreted as the non-penetration boundary condition, and the tangential velocity of the flow on the wall is zero, which is referred as the no-slip boundary condition. They are expressed as,

$$\begin{cases} \mathbf{u}(\mathbf{x}) \cdot \mathbf{n}\big|_{\mathbf{x}\in\partial\Omega_i} = 0 & \text{non-penetration boundary condition} \\ \mathbf{u}(\mathbf{x}) \cdot \mathbf{t}\big|_{\mathbf{x}\in\partial\Omega_i} = 0 & \text{no-slip boundary condition} \end{cases}$$

(11)

where $\mathbf{u}$, $\mathbf{n}$ and $\mathbf{t}$ represent velocity, and unit vectors normal and tangential to the body boundary. Also, there is a free-stream velocity at the far-field which is written as:

$$\mathbf{u}\big|_{\mathbf{x}\to\infty} = \mathbf{u}_\infty$$

(12)

A flow approaches the body with a free stream velocity and no vorticity, then, after passing around the body, the fluid will convect downstream with a non-zero vorticity distribution in the field since vorticities are generated from the body as shown in Fig. 2. Also, the tangential component of the velocity on the surface of the body is canceled by placing a vortex sheet on the surface of the boundary, and the no-slip boundary condition can be then satisfied.

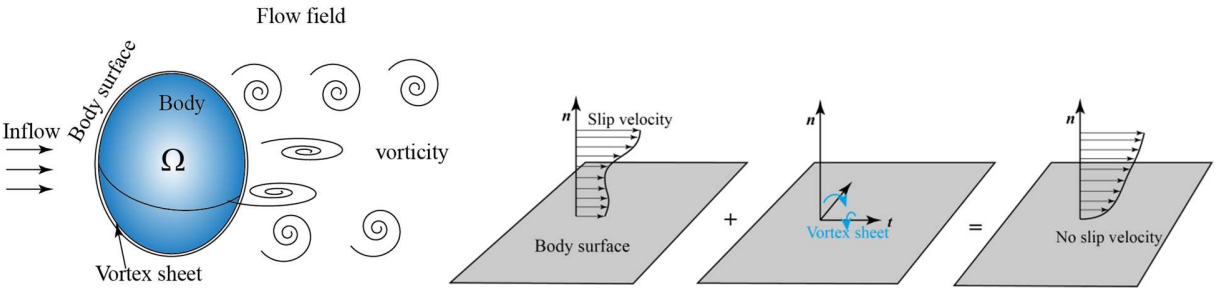

(a) Body boundary (b) Viscous effect

Fig. 2 Schematic of viscous body boundary

If the assumption about the regularity of the velocity field is used, Poincaré's formula [37] can be applied. Thus, inside a body Ω_i :

$$\nabla\times\left(\int_{\partial\Omega_i^-} G(\mathbf{x}-\mathbf{x}')\left(-\mathbf{n}\times\mathbf{u}^-(\mathbf{x}')\right)dS+\int_{\Omega_i} G(\mathbf{x}-\mathbf{x}')\boldsymbol{\omega}(\mathbf{x}')d\mathbf{x}'\right)$$
$$+\nabla\left(\int_{\partial\Omega_i^-} -G(\mathbf{x}-\mathbf{x}')\left(\mathbf{n}\cdot\mathbf{u}^-(\mathbf{x}')\right)dS+\int_{\Omega_i} -G(\mathbf{x}-\mathbf{x}')\left(\nabla\cdot\mathbf{u}(\mathbf{x}')\right)d\mathbf{x}'\right)=\begin{cases}\mathbf{u}(x) & \mathbf{x}\in\Omega_i\\ 0 & x\in\mathbb{R}^3\setminus\Omega_i\end{cases},$$

(13)

and outside a body Ω_i :

$$\nabla\times\left(\int_{\cup\partial\Omega_i^+} G(\mathbf{x}-\mathbf{x}')\left(\mathbf{n}\times\mathbf{u}^+(\mathbf{x}')\right)dS+\int_{\mathbb{R}^3\setminus\cup\Omega_i} G(\mathbf{x}-\mathbf{x}')\boldsymbol{\omega}(\mathbf{x}')d\mathbf{x}'\right)$$
$$+\nabla\left(\int_{\cup\partial\Omega_i^+} -G(\mathbf{x}-\mathbf{x}')\left(\mathbf{n}\cdot\mathbf{u}^+(\mathbf{x}')\right)dS+\int_{\mathbb{R}^3\setminus\cup\Omega_i} -G(\mathbf{x}-\mathbf{x}')\left(\nabla\cdot\mathbf{u}(\mathbf{x}')\right)d\mathbf{x}'\right)=\begin{cases}\mathbf{u}(x) & x\in\mathbb{R}^3\setminus\Omega_i\\ 0 & \mathbf{x}\in\Omega_i\end{cases},$$

(14)

where G is the free-space Green's function.

Because there is no through-flow, the normal velocity on both sides of the boundary is equivalent, $\mathbf{n}\cdot\mathbf{u}^+=\mathbf{n}\cdot\mathbf{u}^-$. Also, an expression for the velocity in the extended domain $\mathbb{R}^3$ can be written by adding the above two equations.

$$\mathbf{u}(x)=(K\times)*\boldsymbol{\omega}_{\cup\Omega_i}-K*\sigma_{\cup\Omega_i}+(K\times)*\boldsymbol{\omega}_{\mathbb{R}^3\setminus\cup\Omega_i}+\int_{\cup\partial\Omega_i} K(\mathbf{x}-\mathbf{x}')\times\boldsymbol{\gamma}(\mathbf{x}')dS$$

(15)

where $\boldsymbol{\omega}_{\cup\Omega_i}$, $\sigma_{\cup\Omega_i}$, and $\boldsymbol{\omega}_{\mathbb{R}^3\setminus\cup\Omega_i}$ are the vorticity inside the body present in the flow, the dilatation $\nabla\cdot\mathbf{u}$ inside the body, and the vorticity present in the flow, respectively. $\boldsymbol{\gamma}=\mathbf{n}\times(\mathbf{u}^+-\mathbf{u}^-)$ is the bound vortex sheet (see Fig. 2) which enforces the no-slip condition, and *K* is a smoothing function as,

$$K(\mathbf{x},\mathbf{x}')=\nabla G(\mathbf{x},\mathbf{x}')$$

(16)

Since bodies, such as the ground or obstacles, are considered to be rigid and do not move in the present work, the first two terms in Eq.(15) can be simplified. The vorticity "inside" the body reduces to zero, and the dilatation is null. The limit of the tangential component of Eq. (15) for $\mathbf{x}\to\mathbf{x}_{\partial\Omega_i^-}$ can be rewritten as

$$\frac{\boldsymbol{\gamma}\times\mathbf{n}}{2}-\int_{\cup\partial\Omega_i}K(\mathbf{x}-\mathbf{x}')\times\boldsymbol{\gamma}(\mathbf{x}')dS=\mathbf{u}_{\text{slip}}$$

(17)

where $\mathbf{u}_{\text{slip}}$ is the third term of the right-hand side of Eq.(15) which is the induced velocity due to the vorticity in the flow field.

Eq.(17) is a Fredholm equation of the second kind which justifies the no-slip condition, and defines the vortex sheet on the surface of the body which is used to generate vorticity inside the flow field as discussed later. Since $\mathbf{u}=\nabla\times\psi$ and $\boldsymbol{\omega}=\nabla\times\mathbf{u}=\nabla\times(\nabla\times\psi)$ with the definition that ψ is the stream function related to $\boldsymbol{\omega}$, the equation

$$\int_{\Omega_i}\psi\cdot\left[\nabla\times(\nabla\times\psi)\right]dV=\int_{\Omega_i}\left|\nabla\times\psi\right|^2dV-\int_{\partial\Omega_i}\psi\cdot\left[(\nabla\times\psi)\times\mathbf{n}\right]dS$$

(18)

can be rewritten as

$$\int_{\Omega_i}\psi\cdot\boldsymbol{\omega}dV=\int_{\Omega_i}\left|\mathbf{u}\right|^2dV-\int_{\partial\Omega_i}\psi\cdot\left(\mathbf{u}\times\mathbf{n}\right)dS$$

(19)

For a nonrotating body, such as the ground or obstacles, $\boldsymbol{\omega}=\mathbf{0}$ everywhere inside it. So, the left-hand side of Eq. (19) vanishes. If $\mathbf{u}\times\mathbf{n}$, the tangential velocity, is also zero at the wall, then Eq. (19) becomes

$$\int_{\Omega_i}\left|\mathbf{u}\right|^2dV=0$$

(20)

This means that the velocity is zero everywhere inside the body and $\mathbf{u}\cdot\mathbf{n}$ vanishes at the wall. In other words, if the no-slip boundary condition is satisfied, then the non-penetration boundary condition is automatically satisfied.

The vortex sheet, $\boldsymbol{\gamma}$, is parallel to the body surface, hence only two of its components need to be determined. By dividing the body surface into vortex sheet panels, integration on the surfaces in Eq. (17) can be equivalently written as the superposition of integrations on the panels that constitute those surfaces. Quadrilateral, constant-strength panels are used in the current study. Therefore, the viscous boundary conditions are transformed to algebraic equations to solve for the vortex sheet distribution.

In a viscous flow, the presence of a solid boundary affects the flow by forcing the fluid to decelerate to zero velocity at the wall. In other words, a solid body is a source of vorticity, and the vorticity generation can be modelled by a flux of vorticity at the body surface [39, 40, and 42]. Therefore, after the vortex sheet on the boundary is obtained to satisfy the no-slip boundary condition, transferring the vorticity of the vortex sheet to the nearby particles in the fluid domain is carried out. This is accomplished solving a diffusion equation with the correct boundary conditions:

$$\begin{aligned}
&\frac{\partial\boldsymbol{\omega}}{\partial t}-\nu\Delta\boldsymbol{\omega}=0,\\
&\boldsymbol{\omega}\left(t-\delta t\right)=0,\\
&\nu\frac{\partial\boldsymbol{\omega}}{\partial n}=\frac{-\boldsymbol{\gamma}(s)}{\delta t}.
\end{aligned}$$

(21)

The solution of Eq.(21) can be computed in its integral form [39].

$$\boldsymbol{\omega}\left(\mathbf{x},t\right)=\int_0^t\int_{\partial\Omega}G_{\mathrm{h}}\left(\mathbf{x},t;\mathbf{s},\tau\right)\boldsymbol{\gamma}\left(\xi,\tau\right)dsd\tau$$

(22)

where G_{h} is the three-dimensional heat kernel, with $\tau<t$

$$G_{\mathrm{h}}\left(\mathbf{x},t;\mathbf{s},\tau\right)=\left(4\pi\nu(t-\tau)\right)^{-3/2}\exp\left(-\frac{\left|\mathbf{x}-\mathbf{s}\right|^2}{4\nu(t-\tau)}\right)$$

(23)

This flux must be emitted during a time Δt. In effect, the vortex sheet $\boldsymbol{\gamma}$ must be distributed to neighbor particles by discretizing the Green's integral for the inhomogeneous Neumann problem corresponding to the diffusion equation. Then, a particle receives, from that panel, an amount of "vorticity × volume" given by

$$\Delta\boldsymbol{\alpha}_i = \int_0^{\Delta t} \frac{d\boldsymbol{\alpha}_i}{dt} dt$$

(24)

with

$$\frac{d\boldsymbol{\alpha}_i}{dt} = \int_{x_i-h_{xi}/2}^{x_i+h_{xi}/2} \int_{y_i-h_{yi}/2}^{y_i+h_{yi}/2} \int_{z_i-h_{zi}/2}^{z_i+h_{zi}/2} \frac{d\boldsymbol{\omega}}{dt} dxdydz$$

(25)

where (x_i, y_i, z_i) and (h_{xi}, h_{yi}, h_{zi}) are the position of the particle and the edge lengths of the integration cuboid, respectively.

The rate of change of the vorticity, $d\boldsymbol{\omega}/dt$, due to a rectangular panel of uniform strength $\boldsymbol{\gamma}$ and size $b \times f$, as shown in Fig. 3, is equal to

$$\frac{d}{dt}\boldsymbol{\omega}(\mathbf{x},t) = \frac{\Delta\boldsymbol{\gamma}}{\Delta t}\frac{1}{2\sqrt{\pi}}\frac{1}{\sqrt{4\nu t}}\exp\left(-\frac{z^2}{4\nu t}\right)\left[erfc\right]_{(x-b/2)/\sqrt{4\nu t}}^{(x+b/2)/\sqrt{4\nu t}}\left[erfc\right]_{(y-f/2)/\sqrt{4\nu t}}^{(y+f/2)/\sqrt{4\nu t}} .$$

(26)

Then,

$$\frac{d\boldsymbol{\alpha}_i}{dt} = \frac{\Delta\boldsymbol{\gamma}}{\Delta t}\left[erfc\right]_{(z_i+h_{zi}/2)/\sqrt{4\nu t}}^{(z_i-h_{i,l}/2)/\sqrt{4\nu t}} \times \frac{1}{2}\sqrt{4\nu t}\left(\left[ierfc\right]_{((x_i-b/2)-h_{xi}/2)/\sqrt{4\nu t}}^{((x_i-b/2)+h_{xi}/2)/\sqrt{4\nu t}} - \left[ierfc\right]_{((x_i+b/2)-h_{xi}/2)/\sqrt{4\nu t}}^{((x_i+b/2)+h_{xi}/2)/\sqrt{4\nu t}}\right)$$
$$\times \frac{1}{2}\sqrt{4\nu t}\left(\left[ierfc\right]_{((y_i-f/2)-h_{yi}/2)/\sqrt{4\nu t}}^{((y_i-f/2)+h_{yi}/2)/\sqrt{4\nu t}} - \left[ierfc\right]_{((y_i+f/2)-h_{yi}/2)/\sqrt{4\nu t}}^{((y_i+f/2)+h_{yi}/2)/\sqrt{4\nu t}}\right)$$

(27)

The time integral in Eq. (27) is evaluated numerically using a Gauss quadrature with four points.

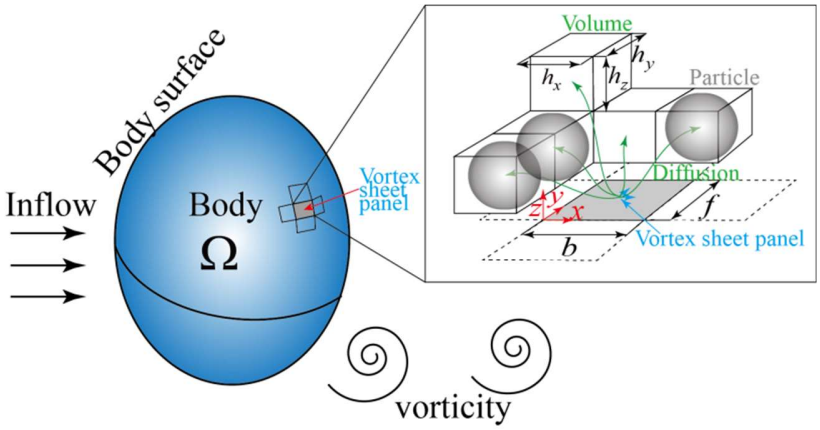

Fig. 3 Diffusion of vorticity of vortex sheet to particles

If the spatial distribution of the particles is not well aligned with the vortex sheet panels, a corrected strength [43, 44] is used to minimize $\sum_i \left|\Delta\boldsymbol{\alpha}_i - \Delta\boldsymbol{\alpha}_{i,conserv}\right|^2 / \left|\Delta\boldsymbol{\alpha}_i\right|^2$ with the constrain that $s\Delta\boldsymbol{\gamma} - \sum_i \Delta\boldsymbol{\alpha}_{i,conserv} = 0$ and enforce conservation via:

$$\Delta\boldsymbol{\alpha}_{i,conserv} = \Delta\boldsymbol{\alpha}_i + \frac{(\Delta\boldsymbol{\alpha}_i)^2}{\sum_j (\Delta\boldsymbol{\alpha}_i)^2}\left(s\Delta\boldsymbol{\gamma} - \sum_j \Delta\boldsymbol{\alpha}_j\right)$$

(28)

where *j* runs over all particles associated with the panel.

Conservation of momentum in the Navier–Stokes equations is expressed as:

$$\frac{\partial \mathbf{u}}{\partial t} + \mathbf{u}\cdot\nabla\mathbf{u} = -\frac{1}{\rho}\nabla p + \nu\nabla^2\mathbf{u}\ .$$

(29)

Taking the dot product of the momentum equation with the tangential vector of the body surface [45, 46], the derivative of the pressure can be expressed as:

$$\frac{D\mathbf{u}_t}{Dt} = -\frac{1}{\rho}\frac{\partial p}{\partial s} - \nu\frac{\partial \boldsymbol{\omega}}{\partial \mathbf{n}}$$

(30)

where *s* and $\mathbf{n}$ denote the tangential and normal outward directions of the surface panel, respectively.

Since the fluid acceleration on the wall must coincide with that of the body under the no-slip condition, and assuming a fixed, rigid body, the Eq. (30) reduces to

$$\frac{1}{\rho}\frac{\partial p}{\partial s} = -\nu\frac{\partial \boldsymbol{\omega}}{\partial \mathbf{n}}$$

(31)

where the right hand side term is the creation of the vorticity on the surface.

An expression for the pressure gradient along the solid boundary can be obtained by combining Eq. (21) and Eq. (31) as

$$\frac{\partial p}{\partial s} = -\rho\frac{\partial \boldsymbol{\gamma}}{\partial t}$$

(32)

The pressure on the body is then obtained by integrating Eq. (32) that only contains the vorticity flux on the surface.

III.Numerical Results and Discussions

The test cases employed here, ranging from an isolated single rotor IGE to a more complex case with an overlapping tandem rotor IGE, are based on a set of well-defined experimental data published in the literature. The tip vortices, and the axial and radial vortex locations of the isolated single rotor IGE are first predicted. The radial velocity profile of a single scale rotor operating in ground effect is then computed. The more complex case with the overlapping tandem rotorcraft IGE is implemented to discuss the DWOW and the wake structure.

A. Trajectories of the Tip Vortices of the Lynx Tail Rotor in Ground Effect

A quantitative verification of the present approach can be obtained by comparing predictions of the trajectories of the tip vortices with the experimental data of Light [47]. This test campaign considered a hovering rotor at different heights above the ground, and was conducted at the Outdoor Aerodynamic Research Facility of the NASA AMES Research Center. The test apparatus consisted of the four-bladed full-scale Lynx tail rotor mounted on the Tail Rotor Test Rig (TRTR). The four-bladed rotor had constant chord, and untwisted blades. Its radius was 1.105m. The airfoil, hover tip Mach number, chord *R*e at blade tip, chord, rotor solidity, and rotational speed were NPL9615, 0.56, 2.3×10^6, 0.18m, 0.208, and 172.82rad/s, respectively. The collective pitch in the present simulations OGE, h/R=1.54, h/R=0.84, and h/R=0.52 were 17°, 15°, 13°, and 15°, respectively, and they were the same as the experiment. A wide-field shadowgraph method captured the tip vortices of the hovering rotor for all heights above a flat board representing the ground. The positions of the vortices were extracted from the shadowgraphs. The blade was modelled with 4800 panels composed of 60 panels in the chordwise direction, and 20 panels in the span-wise direction. The azimuthal angle step was 2.5°. The ground plane was modelled as 8m×8m with 1600 panels and was centred at the rotor axis shown in Fig. 4. The rotor hub was not modelled.

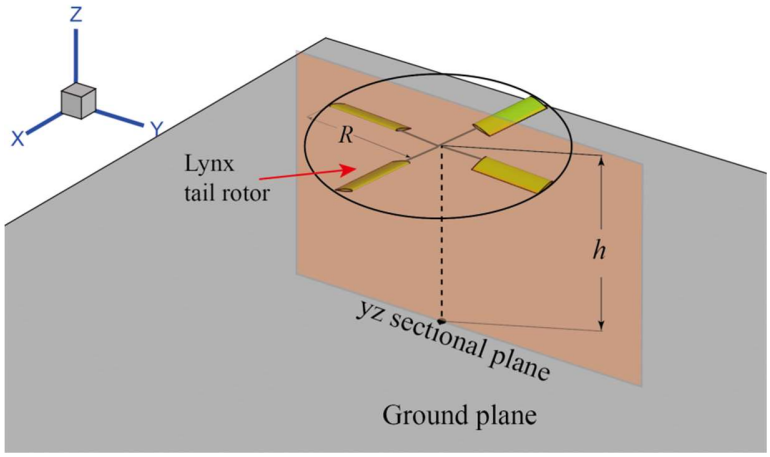

Fig. 4 Schematic of the Lynx tail rotor in ground effect

Table 1 Thrust and power comparison with experiment [47] at different rotor heights

h/R	$C_T/C_{T,\,OGE}$		$C_P/C_{P,\,OGE}$	
	Experiment	Present	Experiment	Present
4.00	1.000	1.000	1.000	1.000
1.92	1.014	1.013	1.010	1.009
1.54	1.031	1.035	1.000	0.991
0.95	1.090	1.083	0.986	0.971

Table 1 compares the predicted thrust and power coefficients with the experimental data at different rotor heights and for constant collective pitch. Note that the values are normalized with the respective OGE values. There is a good agreement between the computational and the experimental results. Also, as expected, the thrust increases with decreasing the rotor height above the ground, while the power slightly decreases, as observed during the experiments.

The trajectories of the tip vortices and the sectional vorticity of the rotor OGE are shown in Fig. 5. The colour range used for the vorticity contours is the same for Figs. 5a and 5b. Also, the axial and radial locations of the tip vortices are shown and compared with the experiments, the vortex transport model (VTM) results [7], and the CFD results [48]. The VTM was a finite volume computational model of the Navier–Stokes equations in vorticity formulation [7]. A lifting-line method was used to simulate the aerodynamics of the rotor blades, and the ground plane was represented by an inviscid mirror-image method in the VTM [7]. The CFD results shown here, were obtained by the FLOWer code and published in the open literature [48]. The rotor is placed approximately 10 rotor radii above the ground to minimize interference from the ground in OGE simulations. The contraction of the tip vortices near the rotor plane, and the unsteady behavior of the far wake are captured by the present method, as

shown in Fig. 5. The CFD over-predicted the radial contraction of the tip vortices and predicted a higher axial descent rate after the first blade passage, while the VTM analysis slightly under-predicted the axial descent rate. There is an excellent agreement between the present predictions and the experiments.

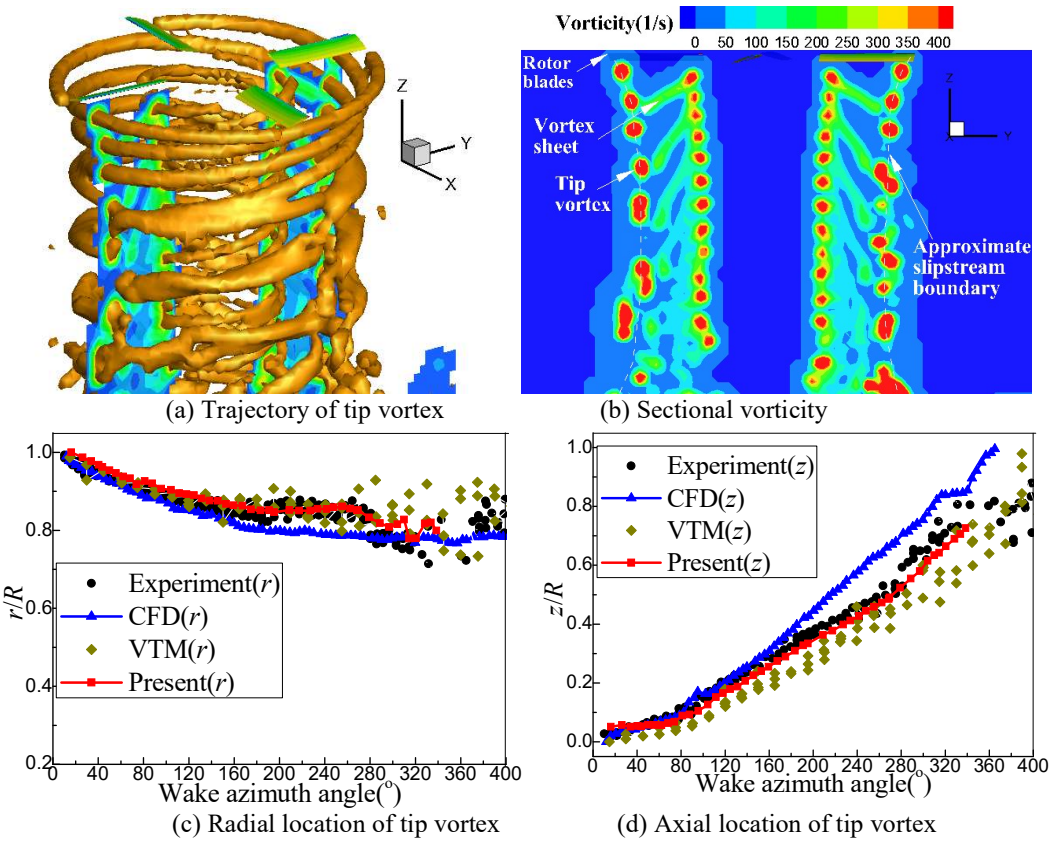

(a) Trajectory of tip vortex (b) Sectional vorticity

(c) Radial location of tip vortex (d) Axial location of tip vortex

Fig. 5 The tip vortex and the sectional vorticity of the Lynx tail rotor OGE

Comparisons of the tip vortex axial and radial locations for different rotor/ground plane separation distances, h/R=1.54, 0.84, and 0.52, of the CFD, the VTM, and the present method are plotted in Fig. 6. It is shown that the CFD had a tendency to over-estimate the wake expansion and axial convection, while the VTM slightly under-predicted the wake contraction and axial descent rate. Nevertheless, a qualitative comparison with the present approach can be made suggesting a satisfactory wake contraction, expansion, and axial convection.

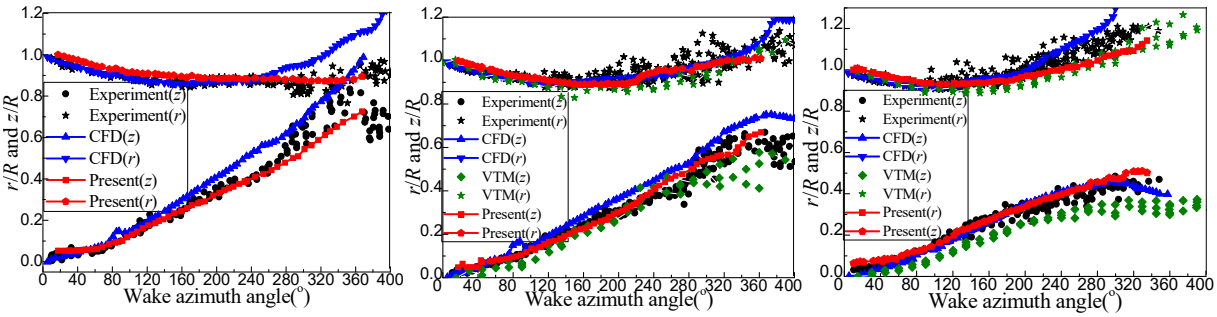

(a) C_T/σ=0.08, h/R=1.54 (b) C_T/σ=0.071, h/R=0.84 (c) C_T/σ=0.09, h/R=0.52

Fig. 6 The tip vortex axial and radial locations of the Lynx tail rotor IGE

The trajectories of the tip vortices (visualized by vorticity iso-surfaces) and the vorticity field around the rotor IGE, and for different rotor/ground plane separation distances, h/R=1.54, 0.84, and 0.52, are shown in Fig. 7. The tip vortices contract in the near wake, and expand in the far wake due to the effect of the ground plane. Additionally, unsteadiness in the far wake is observed.

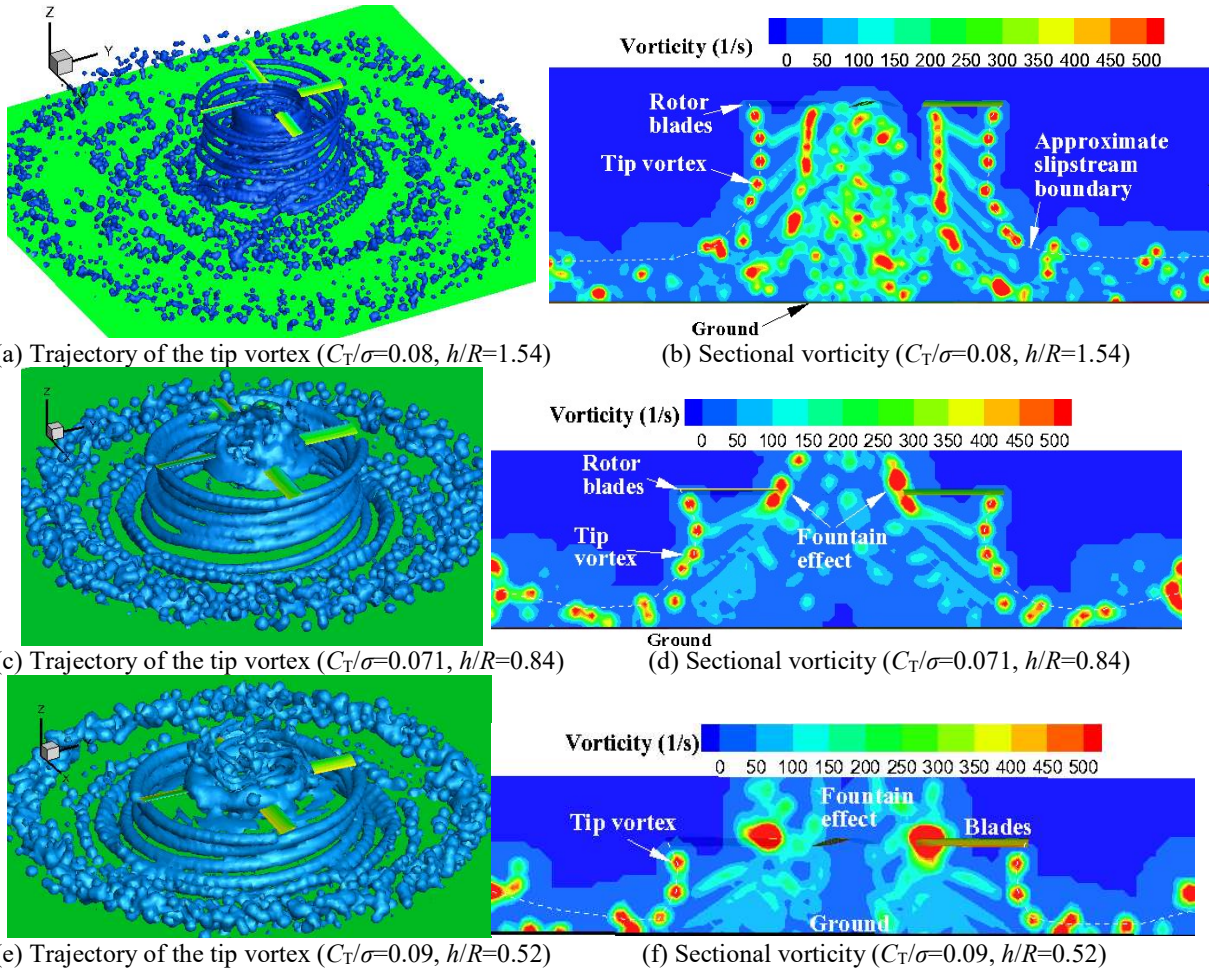

(a) Trajectory of the tip vortex (C_T/σ=0.08, h/R=1.54) (b) Sectional vorticity (C_T/σ=0.08, h/R=1.54)

(c) Trajectory of the tip vortex (C_T/σ=0.071, h/R=0.84) (d) Sectional vorticity (C_T/σ=0.071, h/R=0.84)

(e) Trajectory of the tip vortex (C_T/σ=0.09, h/R=0.52) (f) Sectional vorticity (C_T/σ=0.09, h/R=0.52)

Fig. 7 The tip vortex and the sectional vorticity of the Lynx tail rotor IGE

B. Radial Velocity Profile of an Isolated Single Rotor in Ground Effect

The ability of the present approach to predict the flow field around a rotor in ground effect has been further investigated using the experiments of Lee et al. [5]. The rotor was modelled with two untwisted rectangular blades of circular arc, cambered airfoil sections. The radius of the blade, chord, aspect ratio, and solidity were 86 mm, 19.6mm, 4.39, and 0.14, respectively. The blades were set at a collective pitch of 12°, and the results were obtained at a tip Mach number of 0.08. Also, the rotor tip-path-plane was adjusted so that it was perfectly parallel to the ground plane. The blade was modelled with 2400 panels composed of 60 panels in the chordwise direction and 20 panels in the span-wise direction. The azimuthal angle step was 2.5°. The operating conditions in the present simulation were the same as the experiment, and the Omega, C_T, C_T/σ, and $C_T/C_{T,OGE}$ were 317.2rad/s, 0.01385, 0.0989, and 1.057, respectively. The ground plane was a square plate with 0.8m×0.8m dimensions and was modelled using 1600 panels. It was centred at the rotor axis with h/R=1.5 as shown in Fig. 8(b). The area of the ground plane used in the present work was greater than that of the experiment, and the present model of the ground plane could include the model in the experiment which was a circular disk, three times the diameter of the rotor.

Visualization of the predicted rotor wake is compared with the experiments in Fig. 8 to highlight the structure found within the wake below the rotor. Snapshots of the experimental and predicted flow field show the formation of the tip vortices and the flow structures below the rotor, as well as the wall jet. Furthermore, the tip vortices contract radially inward after shed from the blades, and expand and stretch radially outward as they approach the ground surface. Moreover, the numerical results (see Figs. 8(b) and 8(c)) reveal the onset of vortex pairing for the older vortices. The vortices spin around each other, while the vortex sheets convect axially faster than the blade tip vortices, and interact and merge with the older tip vortices as they age in the flow. Then, they produce a marginally thick wall jet with a variety of eddies of various scales as the ground plane is approached.

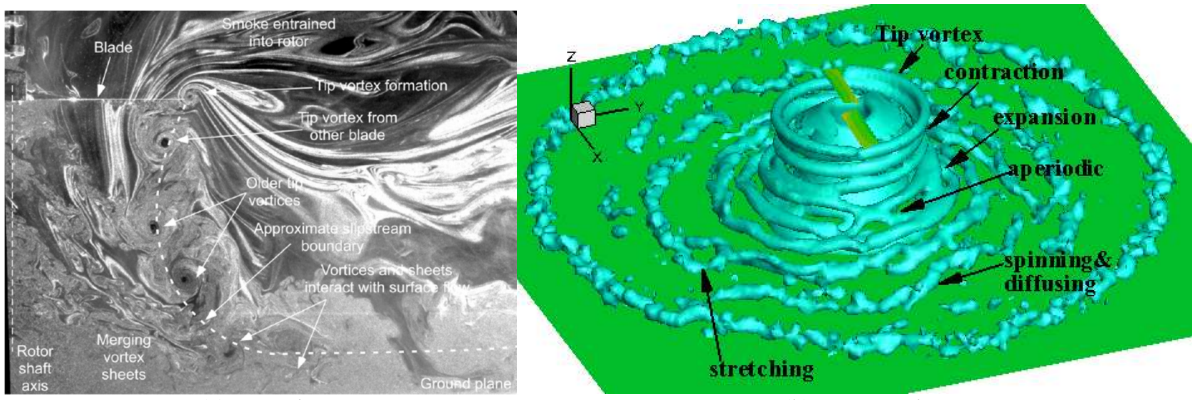

(a) Experiment [5] (b) Rotor wake

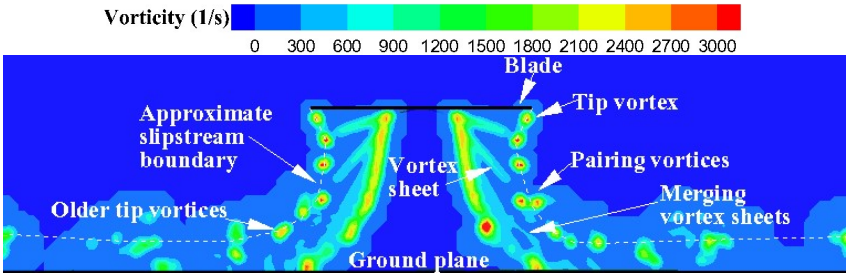

(c) Sectional vorticity

Fig. 8 Flow visualization of the rotor IGE

A more quantitative validation of the present method is carried out comparing the time-averaged radial velocity profiles at six radial distances from the center, r/R=0.8, 1.0, 1.25, 1.5, 1.75, and 2.0, with experimental data and published CFD results [32] in Fig. 9. The velocities are normalized by the ideal hover induced velocity for the corresponding thrust coefficient with 0.01385. Published CFD results of the OVERTURNS solver are used for comparisons. The OVERTRUNS is a widely used, validated and documented tool [32]. Fig. 9 shows that the time-averaged velocities predicted using the present method have similar trends as the experiment and the CFD. The estimated time-averaged velocities match well with the CFD results at r/R=0.8, 1.0, and 1.25, while both the present method and the CFD under-predict the peak radial velocities. The peak radial velocities at r/R=1.5 and 1.75 were over-predicted by the CFD method, whereas they are under-predicted by the present method. Additionally, the peak radial velocity at r/R=2.0 was over-predicted by the CFD method, whereas the present prediction compares satisfactorily with the experiment. There are negative radial velocity excursions at and downstream of r/R=1.5 since the tip vortices are pushed outward as they approach the ground plane, while those tip vortices induce a negative radial velocity above the thickness of the wall jet. Also, both the CFD and the present method predict a maximum radial velocity at a similar wall distance which is slightly larger than that of the experiments. It should be noted that even though there are discrepancies due to the interaction of the tip vortex with the ground plane, the overall comparisons between the present results, the CFD results, and the experiments are still acceptable. Moreover, the CPU time of the CFD and the present method is shown in Tab.2. It should be noted that, contrary to the CFD, the present method is more efficient.

Table 2 CPU time of the CFD and the present method

Method	Revolutions	CPU	Computer	CPU time (hours)
CFD	18	Intel Xeon 3.2GHz	Cluster	2000 per million grid points [32]
Present	20	Intel i7-3770 3.4GHz	Desktop	58

Figure 9 shows what is usually interpreted as the formation of a radial wall jet as the wake impinges on the ground. The computations correctly predict the overall physics of the flow field. The rotor induced flow is forced to expand radially outward, creating the wall jet. The height of the wall jet is seen to decrease as one moves radially outward, which is similar to the experimental data. This is because the flow turns from vertical in the contraction region to horizontal in the outwash region with increasing distance from the center. As a consequence, there is an increase in the peak radial velocity as the radial distance increases, until it eventually begins to decrease at the outermost measured radial distance.

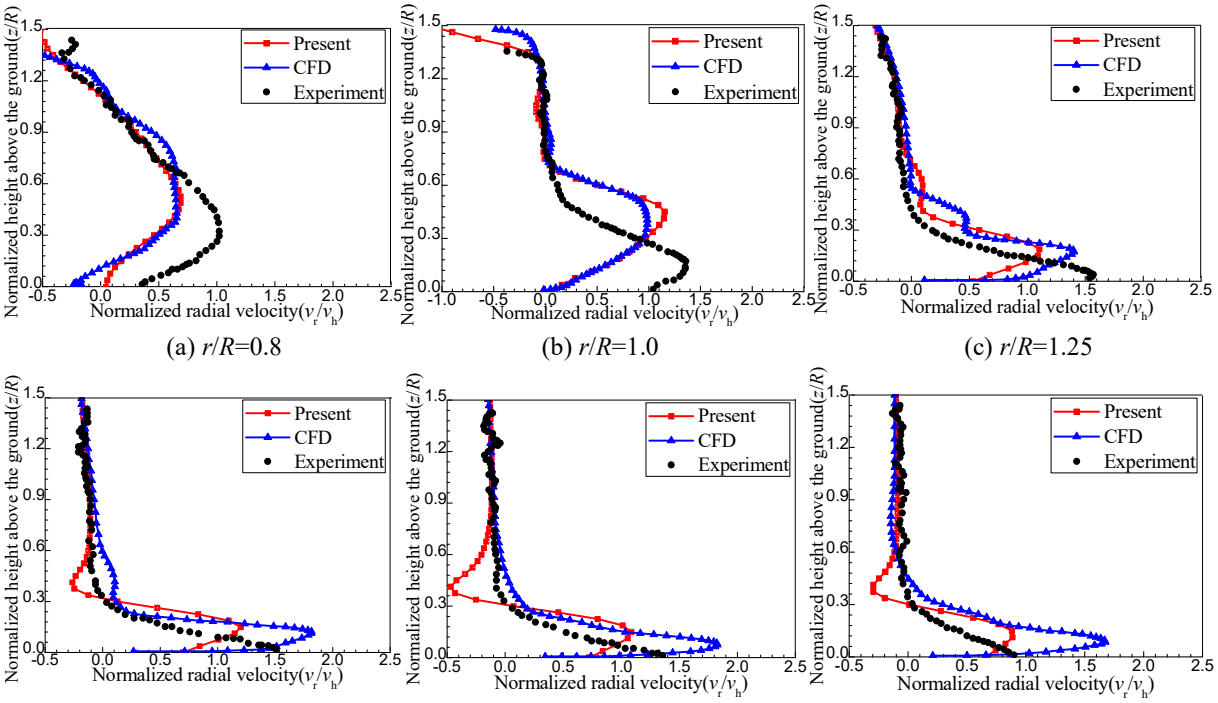

(a) r/R=0.8 (b) r/R=1.0 (c) r/R=1.25

(d) r/R=1.5 (e) r/R=1.75 (f) r/R=2.0

Fig. 9 Time-averaged velocity profiles at different radial distances from the center (IGE)

C. Downwash of the Single Aft Rotor Out of Ground Effect

As opposed to the previous case with a single rotor, DWOW of an overlapping tandem rotor configuration is not axisymmetric since the flow along the longitudinal axis is different from the lateral axis. Also, the interactions of the forward outflow with the aft rotor, and of the vortices from the two rotors with each other and with the inboard vortex sheet, produce a highly complex flow field.

Further verification of the present method can be obtained by examining the downwash and outwash characteristics of the overlapping tandem rotor (model-scale CH-47D) IGE. The experiments were conducted in the U.S. Army hover chamber (25- by 25- by 30-ft high) at the NASA Ames Research Center. The model aircraft CH-

47D was of approximately 1/56th-scale. The forward and aft rotors consisted of three blades with a low Reynolds number airfoil. The rotor blade planform and twist were similar to the equivalent full-scale CH-47D blade. The radius of the blade, solidity, rotor-rotor distance, and tip speed were 6.31in, 0.057, 8.33in, and 194.9ft/s, respectively. The three-bladed hubs rotated counter-clockwise for the forward rotor and clockwise for the aft rotor, as viewed from above. Both rotors were at the same height above the ground plane as the experiment as shown in Fig. 10(c), which were also similar to the full-scale CH-47D hover configuration of Ref. 9 as shown in Figs. 10(a) and 10(b). For the model aircraft, the shaft angles of the forward and aft rotors were 2.5° (forward tilt) and 0°, respectively. The target aircraft C_T was achieved by ensuring equal thrust-sharing between the two rotors, and maintained at approximately C_T=0.0061. The flow field of the model-scale tandem rotor IGE was investigated using PIV.

The rotors were modelled as rigid hubs with collective control only, no cyclic pitch control, or differential collective pitch were used to establish the desired aircraft center of thrust in hover or to trim the pitching moment. Also, the fuselage and the hub of the aircraft, and the load cells were not included in the present simulation. Each computational rotor was modelled with 3600 panels composed of 60 panels in the chordwise direction, 20 panels in the span-wise direction, and the azimuthal angle step was 5.0°. The ground plane was modelled as 2.0m×2.0m with 6400 panels and was centered at the centre of the aircraft shown in Fig. 10.

(a) CH-47D in hover [9]

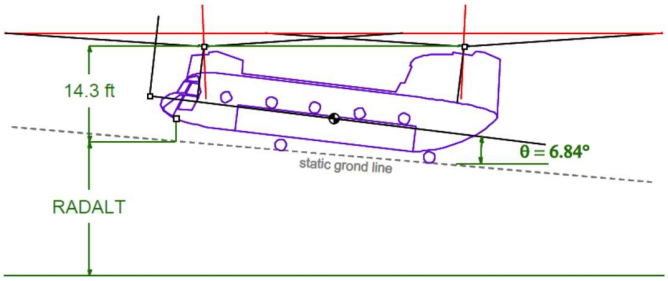

(b) Attitude of CH-47D in hover [9]

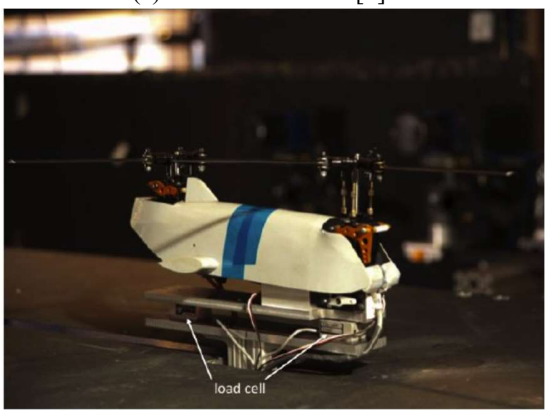

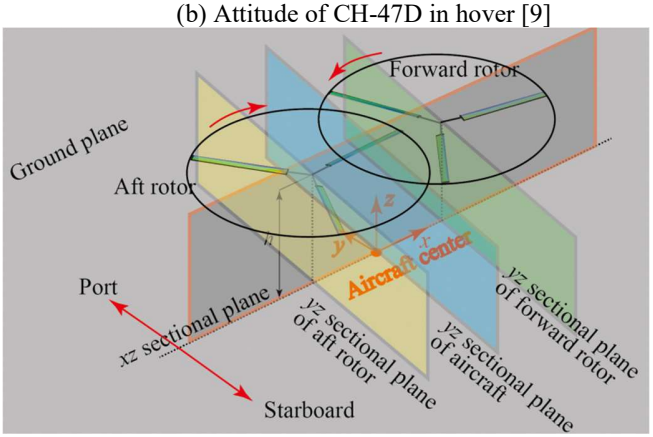

(c) Experimental model [10] (d) The present model

Fig. 10 Model of the tandem rotor

The downwash distribution for the baseline single rotor, which is the aft rotor in the tandem rotor, operating out of ground effect is first computed in this part. The single aft rotor configuration is achieved by removing the forward rotor, thereby removing any effect of blade overlap on the inflow distribution. The predicted flow field of the single aft rotor configuration is plotted in Fig. 11 and compared with the experiments. Note that the contours correspond to downwash velocity normalized using the theoretical hover induced velocity, $V_h = \sqrt{C_T / 2}$. It is seen that the overall flow velocity is predicted reasonably well for this configuration. In addition, the peak velocity at the mid-span of blade is consistent with the experiment.

Comparisons of the downwash velocity profiles with the experiments are shown in Fig. 12. The predicted peaks of the downwash velocity and their corresponding locations are found to match very well with the experimental data. Additionally, the rapid changes of the downwash near the blade tip (see Fig. 12) show the effect of the tip vortices which are captured by the present method. However, the velocity at the root of the blade is not well-predicted since the rotor hub is not modelled. Note that the overall comparison of the downwash velocity at different downstream and radial distances from the center is still very good.

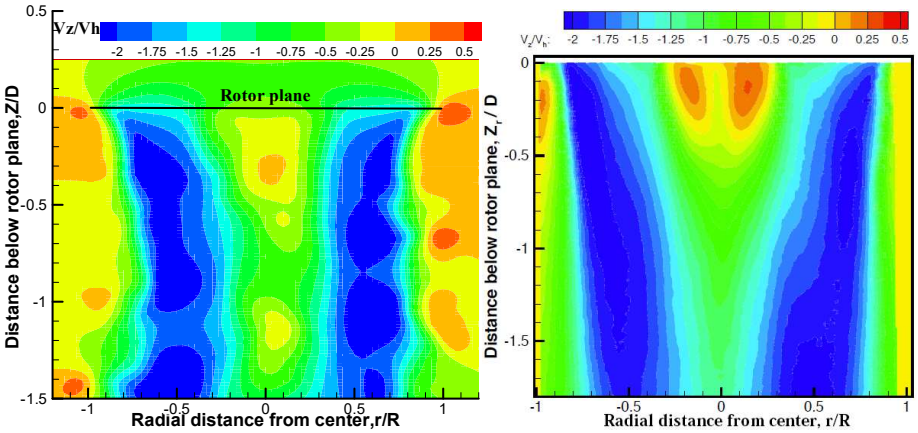

(a) Present (b) Experiment [10]

Fig. 11 Flow field of the single aft rotor OGE

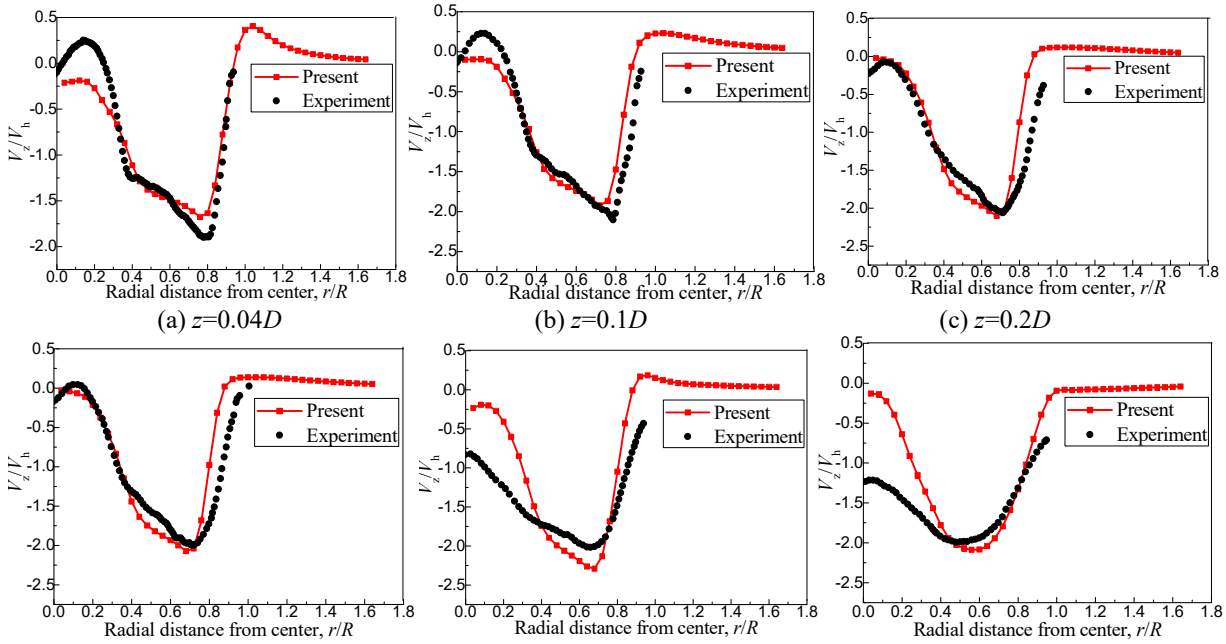

(a) z=0.04D (b) z=0.1D (c) z=0.2D

(d) z=0.4D (e) z=0.5D (f) z=1.0D

Fig. 12 Downwash velocity of the single aft rotor OGE

D. DWOW of the Single Aft Rotor in Ground Effect

Figure 13 shows the downwash velocity distribution at three radial distances, r/R=0.6, 0.75, and 0.8, for the single aft rotor IGE (h/R=1.156). In general, there is good agreement between the computational and the experimental results. The downwash velocity at r/R=0.6 is slightly over-predicted due to the absence of the rotor hub, the fuselage, and the load cells. At r/R=0.75 and 0.8 the predictions are much better. Furthermore, as expected, the predicted maximum downwash velocity which corresponds to the location of maximum wake contraction occurs at the same, z/D≈0.4, for all three radial distances.

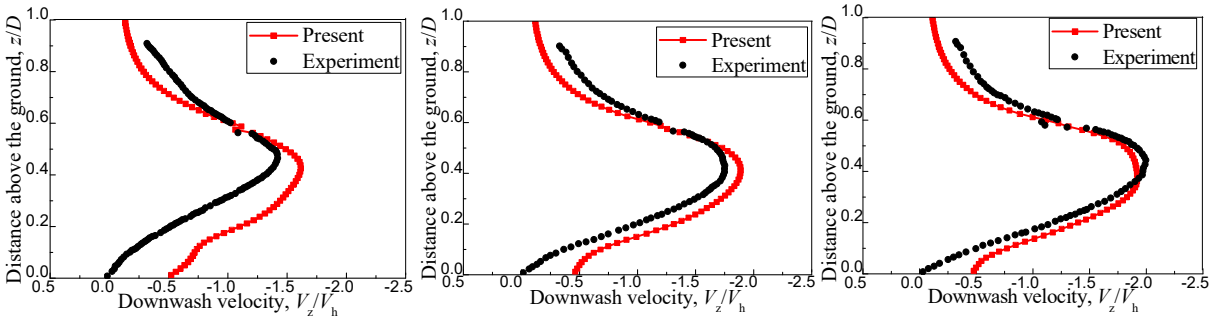

(a) r/R=0.6 (b) r/R=0.75 (c) r/R=0.8

Fig. 13 Downwash velocity at various radial distances from the center for the single aft rotor IGE (h/R=1.156)

The vertical and horizontal components of the velocities at the waist location, z/D≈0.4, across the rotor disc for this configuration are plotted in Fig. 14. Also, experimental data [10, 11] and the CFD results of the Helios solver

[10] are compared with the present approach. The CFD predictions were made for the isolated single rotor configuration at full-scale Reynold number. For this single rotor configuration, a total of 10.6 million grid points were used to model the ground, while the rotor mesh included 10.5 million grid points. Adaptive Mesh Refinement (AMR) was also employed to capture the tip vortices and vortical interactions with the ground with up to 450 million grid points. The predicted vertical velocity distribution, in Fig. 14, shows similar trends as the experiments and the CFD results. Outboard of the rotor blade, it is shown that the peak downwash velocity predicted by the CFD solver was lower by about 20%, suggesting that the wake was slightly less contracted and wider. The peak downwash velocity is predicted correctly by the present approach, indicating that the wake contracts as in the experiments. Moreover, in the inboard region, the upwash was slightly under-predicted by the CFD, while it is slightly over-predicted by the present method, since the hub of the rotor is absent. It should be noted that the upwash in the root region confirms the existence of a vertical flow stream.

The horizontal component of the downwash velocity beneath the rotor disc for this configuration is shown in Fig. 14(b). There is an excellent correlation between the present prediction and the experiments at radial distances from r/R=0.5 to 1.6. However, the velocity at radial distances less than r/R=0.5 is over-predicted by the present method because the rotor hub, the fuselage, and the load cells are not modelled.

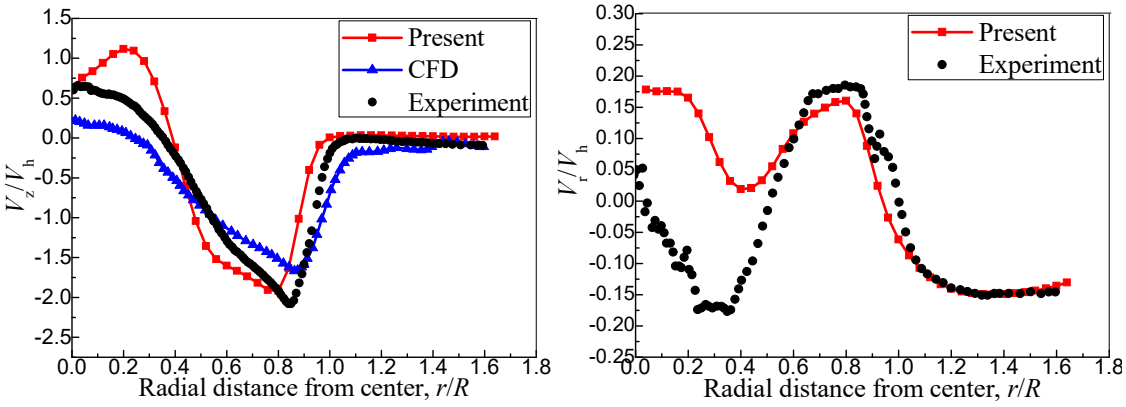

(a) Vertical velocity (b) Horizontal velocity

Fig. 14 Velocity at the waist location (z/D=0.4) for the single rotor IGE (h/R=1.156)

The predicted horizontal velocity component, V_r, is plotted against normal distances from the ground, z/D, at several radial distances and compared with the experimental data as shown in Fig. 15. The peak radial velocity at r/R=0.8 is over-predicted, while at r/R=1.6 it is under-predicted. The distance above the ground plane corresponding to the peak radial velocity which indicates the edge of the wall jet is predicted reasonably well. The peak of the

radial velocity increases as the radial distance increases from the rotor axis to 1.2R, while the thickness of the wall jet decreases.

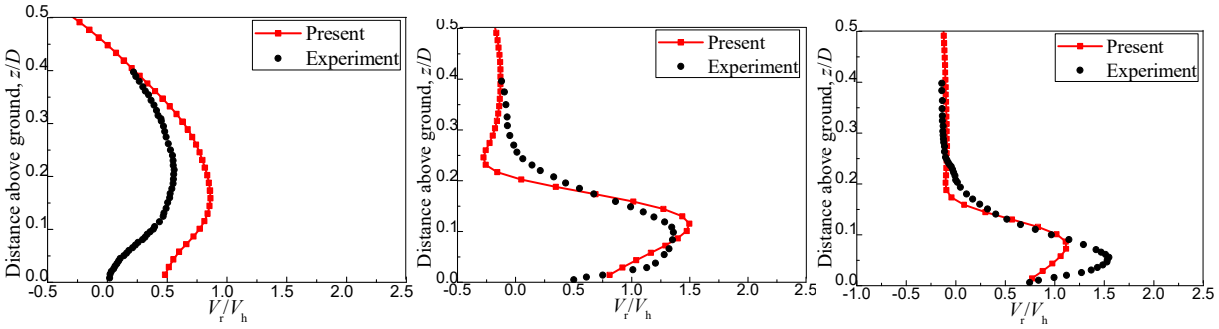

(a) r/R=0.8 (b) r/R=1.2 (c) r/R=1.6

Fig. 15 Radial velocity at various radial distances from the center for the single aft rotor IGE (h/R=1.156)

Figure 16 shows a comparison of the rotor wake of the single aft rotor OGE and IGE (h/R=1.156). Clearly, contrary to the OGE case, the wake distortion becomes particularly pronounced, and the wake quickly expands radially outward after the first rotor revolution as it approaches the ground surface. As a result, the radius corresponding to the peak of vertical velocity at the waist location, z/D=0.4, is significantly pushed outward as shown in Fig. 17. The tip vortices, shown in Fig. 16, are axially closer together than for the OGE case and exhibit some evidence of pairing. Consequently, the rotor operating IGE produces less downwash velocity than the isolated rotor running OGE, which is also confirmed in Fig. 17.

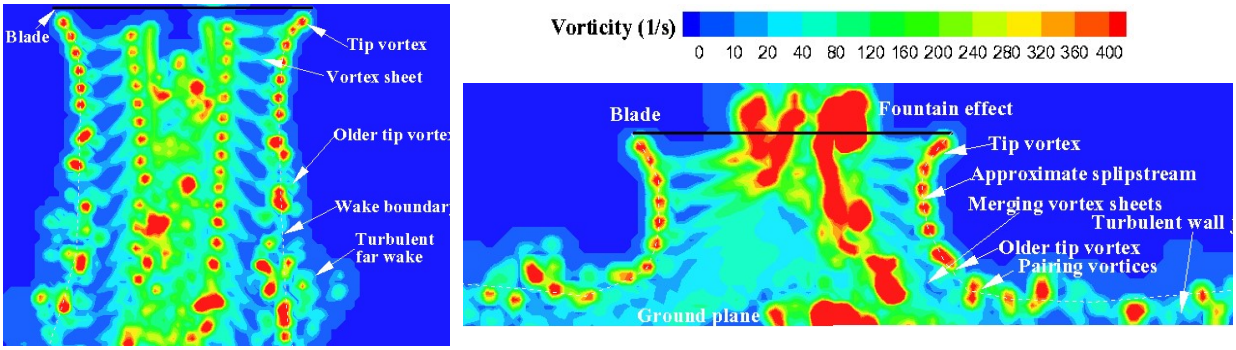

(a) OGE (b) IGE

Fig. 16 Flow visualization of the single aft rotor OGE and IGE (h/R=1.156)

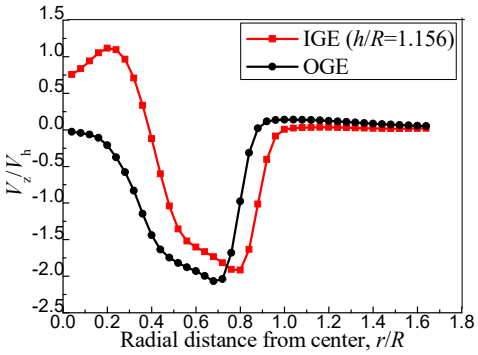

Fig. 17 Velocity at the waist location (z/D=0.4) below the single aft rotor

E. DWOW of the Tandem Rotor in Ground Effect

The DWOW of the overlapping tandem rotor system is more complex than that of the single rotor. The CFD results of Ref.10 were only for the isolated single rotor in ground effect, and there were no results for the tandem rotor. This could be due to the enormous grids and CPU time required.

Figure 18 shows the downwash velocity distribution at the *xz* sectional plane at r/R=0.75 for the tandem rotor in ground effect (h/R=1.156). The results show similar trends as the experimental data. The downwash velocities of the forward and aft rotors are slightly over-predicted due to the absence of the rotor hub and fuselage. Also, the predicted maximum downwash velocity indicates the location of maximum wake contraction occurring at the same, z/D≈0.4, for both the forward and aft rotors. Additionally, the forward and aft rotors also show maximum wake contraction similar to that of the single aft rotor shown in Fig. 13. The satisfactory agreement with the measurements suggests that the wake contraction of the overlapping tandem rotor is well predicted by the present method. However, the velocity close to the ground shows deviations from the experiments. This is probably due to the fuselage which may affect the rotor downwash, but is not modelled in the present simulation.

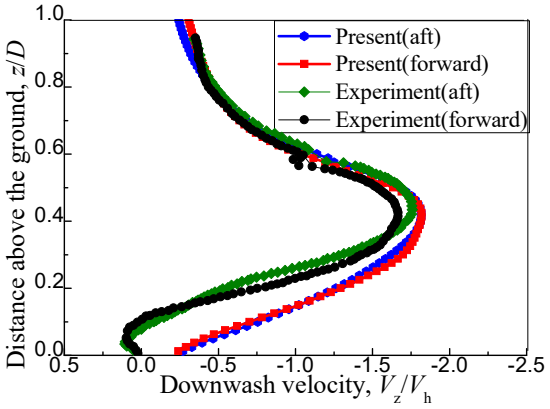

Fig. 18 Downwash velocity at r/R=0.75 for the tandem rotor

The vertical and horizontal components of the velocities extracted from the *xz* sectional plane at the waist location, $z/D \approx 0.4$, which corresponds to the maximum wake contraction, across the rotor disc for the overlapping tandem rotor is shown in Fig. 19. Experimental measurements are also plotted for validation. It is shown that the overall vertical velocity distribution is found to match well with the experiment data. Outboard of the rotor blade, the peak downwash velocity is accurately predicted, indicating that the wake contracts as in the experiments. In the inboard region, the upwash is under-predicted by the present method since the rotor hub and the fuselage are absent. Overall, the numerical predictions for the vertical and horizontal velocities are in fair agreement with the experiments. It should also be noted that the downwash velocity of the forward rotor is slightly lower compared to that of the aft rotor due to the slight inclination of the forward rotor shaft.

The comparison of the horizontal component of the downwash velocity beneath the rotor disc for this configuration in Fig. 19(b) provides some insight into the trend of the outwash which plays a significant role in the brownout. This is because the outwash velocity of the rotor pulls items, such as sand or dust, towards or away from the rotorcraft. There is a good correlation between the present prediction and the experimental measurements for both the forward and aft rotors. And the variation of the outwash in the spanwise direction, which indicates the outwash or in-wash, is captured reasonably well. Additionally, the V_r changes to positive indicating the flow is outward at the tandem rotor with increasing the radial distances from r/R=0.5 to 1.0, while at radial distances from r/R=1.0 to 1.6, the V_r comes back to negative, suggesting the flow is towards the rotorcraft.

For the tandem rotor, the distributions of the vertical and horizontal velocities at the *xz* sectional plane, shown in Fig. 19, indicate similar trends as the single aft rotor operating IGE (shown in Fig. 14). The radius corresponding to the peak of the vertical velocity at the waist location, 17%*D* below the rotor, across the rotor disc is also pushed outward as shown in Fig. 17 in comparison to the single aft rotor operating OGE. Furthermore, the tandem rotor operating IGE also produces less downwash than the single aft rotor operating OGE. Contrary to the single aft rotor, the peak of the horizontal velocity of the aft rotor under the effect of blade overlap is larger, which indicates comparable or greater outwash than that of the single aft rotor. The reason for this difference is explained by the strong wake interaction between the forward and aft rotors, which will be confirmed later.

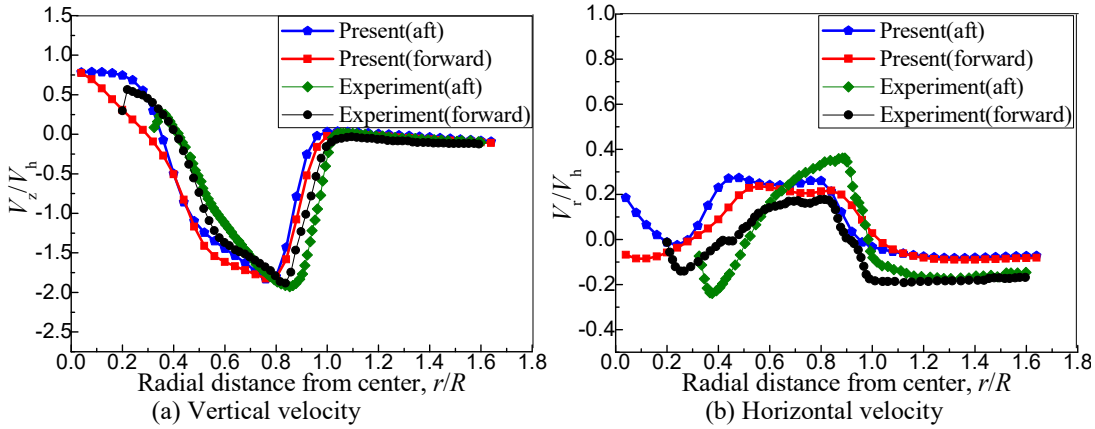

Fig. 19 Velocity at z/D=0.4 (xz sectional plane) for the tandem rotor IGE (h/R=1.156)

The predicted horizontal velocity component, V_r, at the xz sectional plane is plotted against normal distance, z/D, from the ground and compared with the experimental data shown in Fig. 20. It can be seen that, in general, the predicted outwash velocity profiles have similar trends as the measurements. The distance above the ground plane corresponding to the peak radial velocity in the outboard region is predicted reasonably well, which indicates that the thickness of the wall jet can be captured by the present method. Also, the peak radial velocity at r/R=0.8 is over-predicted, while it at r/R=1.2 and 1.6 is under-predicted. Even though there are discrepancies, the simulation validated against the overlapping tandem rotor for DWOW shows acceptable agreement. Moreover, the height corresponding to the peak outwash velocity of the aft rotor is greater compared to that of the forward rotor, suggesting that the wall jet of the aft rotor is thicker than that of the forward rotor. This is because the inclination of the forward rotor produces velocity vectors at an angle. Additionally, contrary to the single aft rotor IGE shown in Fig. 15, the peak of the radial outwash of the aft rotor under the effect of the forward blade overlap is greater. Moreover, the height corresponding to the peak outwash velocity of the tandem rotor is greater than that of the single rotor. Those changes are mainly caused by the strong wake interaction between the forward and aft rotors.

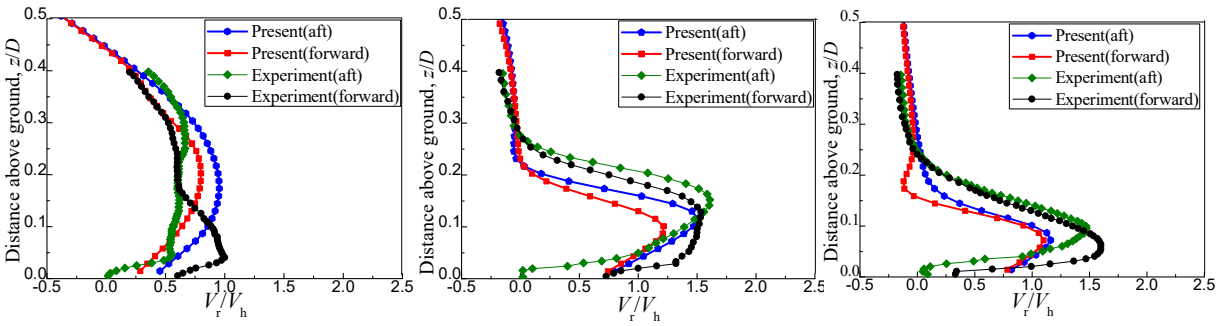

Fig. 20 Radial velocity at different radial distances (xz sectional plane) for the tandem rotor IGE (h/R=1.156)

Figure 21 shows the comparison of the time averaged flow field at the *xz* sectional plane of the single rotor and the tandem rotor operating IGE. The color contours correspond to the downwash and outwash velocities normalized using the averaged hover-induced velocity, $V_h = \sqrt{C_T / 2}$. Similar to the single rotor, the radial outward expansion of the forward and aft rotors caused by the effect of the ground plane is observed in Fig. 21(b). And a fountain flow of the aft rotor indicated by the upwash at the blade root is also presented in Fig. 21(d). Contrary to the isolated single rotor, the fountain flow of the aft rotor is clearly strengthened in Fig. 21(d). There are two possible reasons. The first reason could be due to the inclination of the forward rotor. The forward rotor pushes its wake to the center of the aft rotor and forces the vortices of the aft rotor to convect upstream, strengthening the fountain effect. The second reason could be due to the tip-root vortex interaction in the overlapping area between the forward and aft rotors. The tip vortex of the forward rotor is close to the root vortex of the aft rotor and induces an upward velocity on it. As a result, the root vortex of the aft rotor is then pushed upwards. Moreover, on the both sides of the overlapping area, radial outward expansions are also obviously observed in Figs. 21(b) and 21(f). The reason for this phenomenon is again explained by the interaction of the tip vortices of the forward and aft rotors. In addition to the outward flow, two tip vortices with opposite directions indicated by the change of the direction of the velocity are observed in Fig. 21(b) in the overlapping area of the tandem rotor.

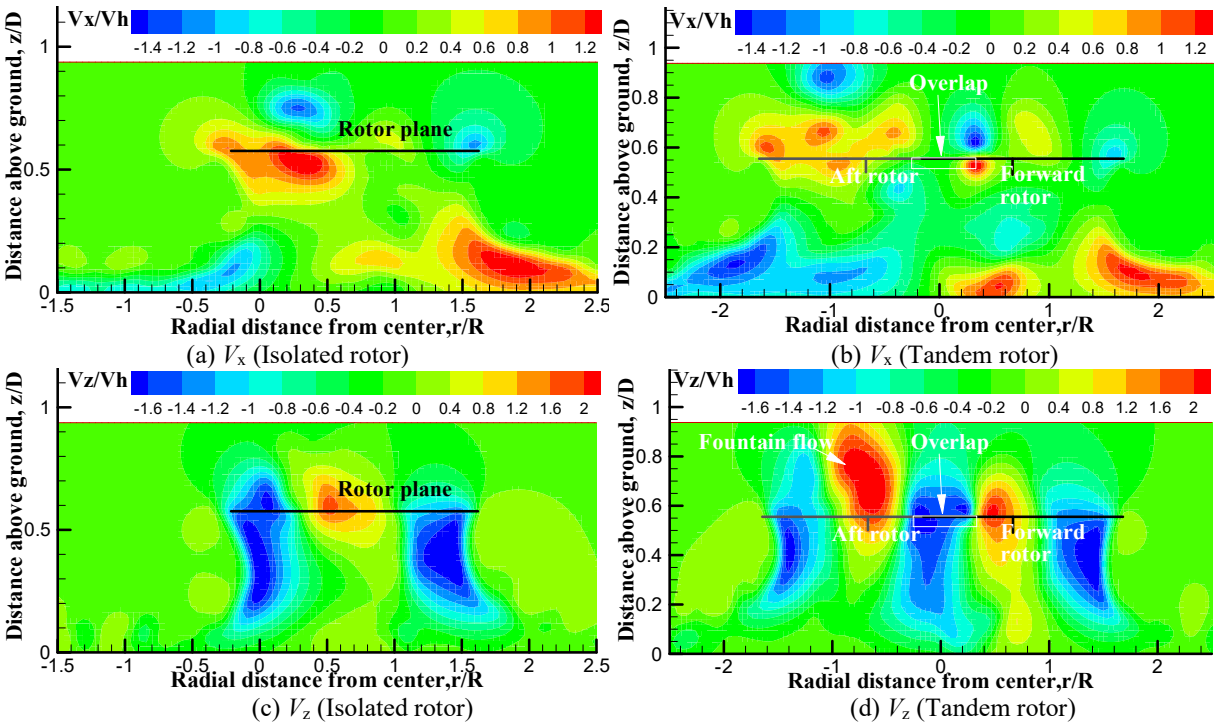

(a) V_x (Isolated rotor)

(b) V_x (Tandem rotor)

(c) V_z (Isolated rotor)

(d) V_z (Tandem rotor)

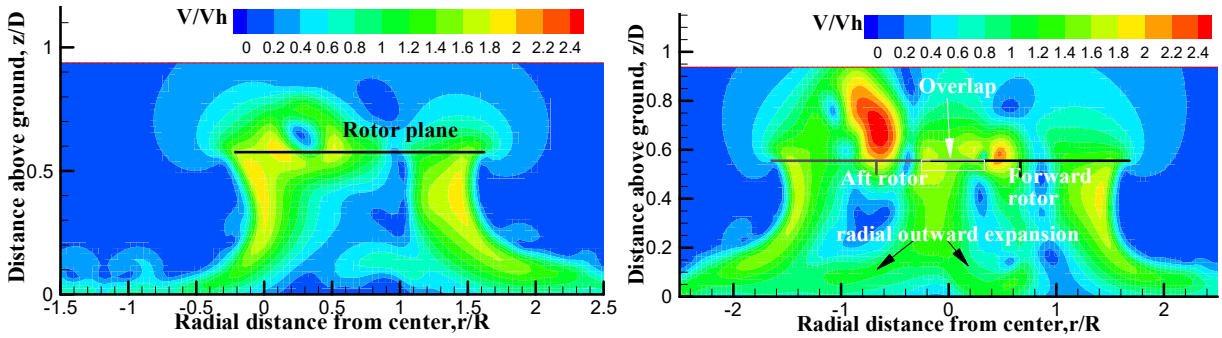

(e) Velocity of in-plane (Isolated rotor) (f) Velocity of in-plane (Tandem rotor)

Fig. 21 Flow field of the single aft rotor and the tandem rotor IGE (*h*/*R*=1.156) at the *xz* sectional plane

The horizontal velocity component, V_r, on the starboard and port sides of the tandem rotor at the *yz* sectional plane of the aircraft is shown against the normal distance, z/D, from the ground and compared with the experiments in Fig. 22. The predicted outwash shows similar trends as the measurements. The distance above the ground plane corresponding to the peak radial velocity is predicted well, indicating that the thickness of the wall jet in the lateral axis can be captured by the present method. Additionally, it is shown that the horizontal component on the both sides of the rotorcraft is quite different. Inside the rotor plane, Fig. 22 (a), the radial velocity, V_r, on the port side is negative over most of the region indicating that the flow moves towards the tandem rotor, whereas the starboard side shows the flow moving away from the rotorcraft below the rotor plane. Therefore, on the starboard side, the merged flow over the overlap region gradually changes direction as it approaches the ground plane. Conversely, the flow on the port side convects vertically until very close to the ground plane, which is confirmed by Fig. 23. This is because the forward and aft rotors are running in opposite directions resulting in a tangential outward velocity on the starboard side while the opposite happens on the port side. Furthermore, in the overlapping area, Fig. 22(a), the radial velocity on the starboard side is greater than that of the port side. Outside the rotor plane and slightly above the thickness of the wall jet, Fig. 22(b), the port side shows higher radial velocity. This is because the tip vortices of the forward rotor will merge with that of the aft rotor on the port side due to the anti-clockwise rotation of the forward rotor and the clock-wise rotation of the aft rotor, while the tip vortices of the forward rotor are far away from that of the aft rotor on the starboard side. As a result, the vorticity of the aged vortex near the ground plane is strengthened, and a greater radial velocity is induced on the port side. Contrary to the starboard side, the thickness of the wall jet on the port side is larger. This is confirmed in Figs. 23, 24(c), and 25(b).

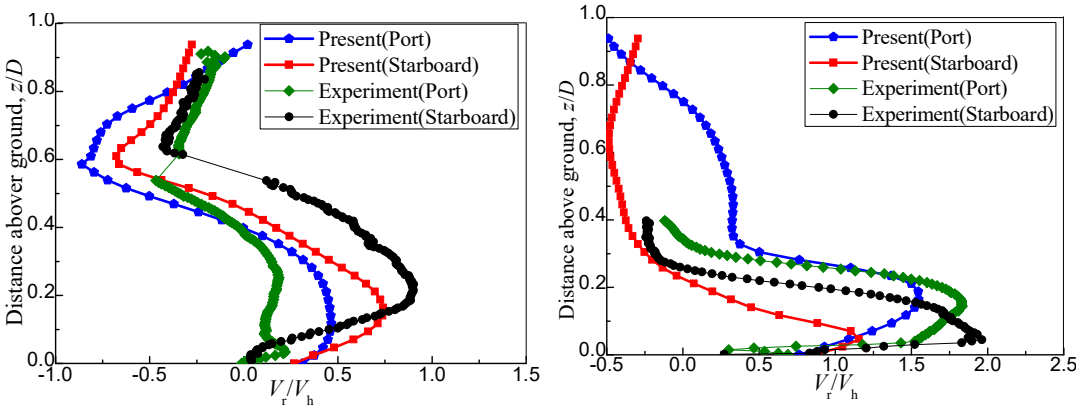

(a) r/R=0.56 (b) r/R=1.2

Fig. 22 Outwash velocity of the tandem rotor IGE (h/R=1.156) at the yz sectional plane of the aircraft

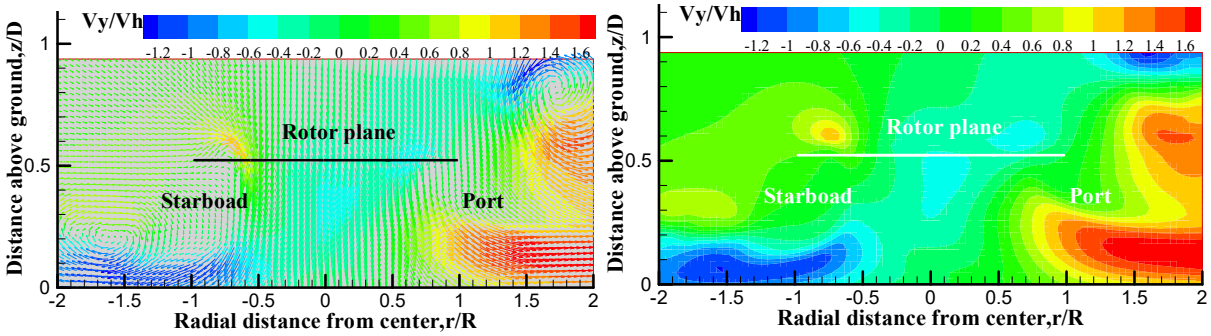

(a) Stream vector (b) Flow field

Fig. 23 Time averaged flow field of the tandem rotor IGE (h/R=1.156) at the yz sectional plane of the aircraft

The predicted wake structure of the tandem rotor wake in IGE visualized by iso-surfaces of vorticity is shown in Fig. 24 and Fig. 25 to highlight the wake structure below the rotorcraft. Similar to the single rotor in ground effect, the tip vortices of the forward and aft rotors contract radially inward after shed from the blades, and expand significantly outward as they approach the ground plane. The fountain effect is also observed near the root of the aft rotor. As opposed to the single rotor, the tip vortices of the tandem rotor on the port side impinge on each other with a tangential inward velocity (shown in Fig. 25) resulting in a different outwash velocity on the port and starboard sides. The observed difference in the vortex pattern can be explained by the rotational direction of the two rotors. Because the rotors are spinning in opposite direction, the swirl pushes the wake outward from the rotorcraft center on the starboard side and inward on the port side which strengthens the tip vortices interaction between the forward and aft rotors. Contrary to the aft rotor, the fountain effect of the forward rotor is weakened due to its inclination. Additionally, interaction of the aft rotor tip vortices and inboard sheet with the forward rotor results in a lager downwash and radial outwash in the overlapping area as shown in Fig. 21; a phenomenon not seen for the single rotor.

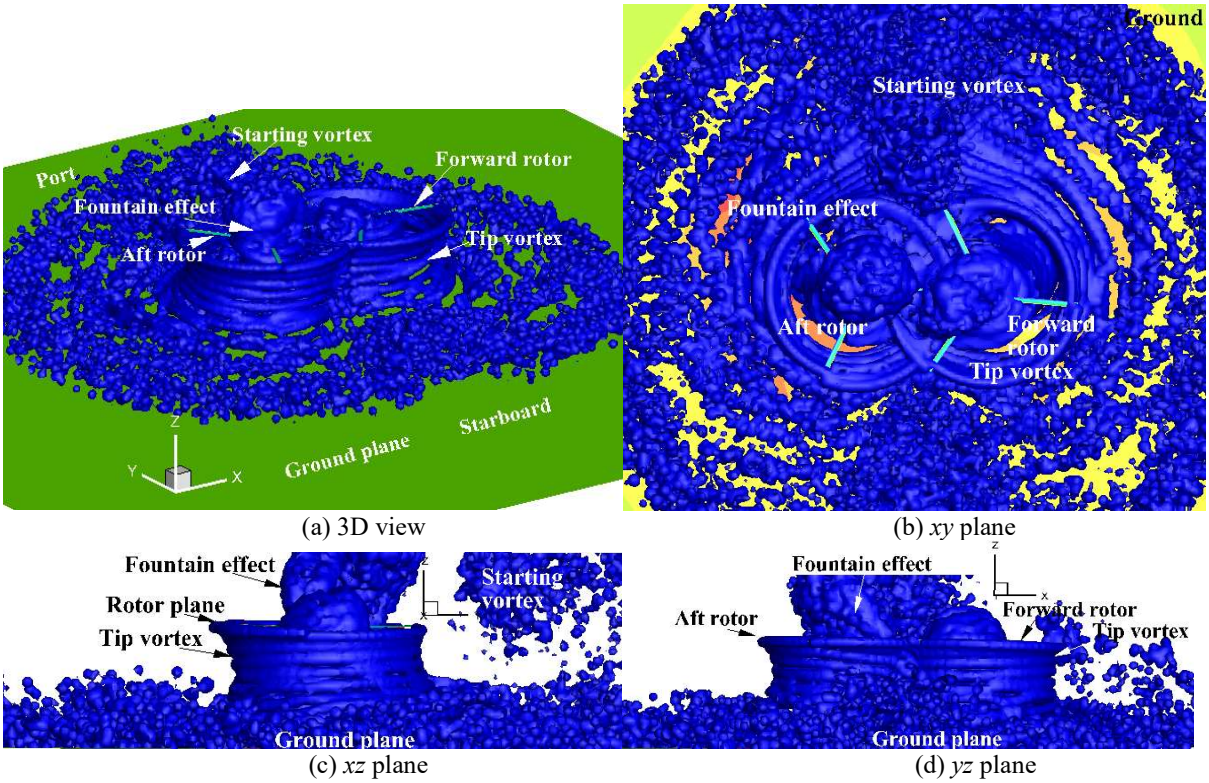

(a) 3D view (b) *xy* plane

(c) *xz* plane (d) *yz* plane

Fig. 24 Wake structure of the tandem rotor IGE (*h*/*R*=1.156)

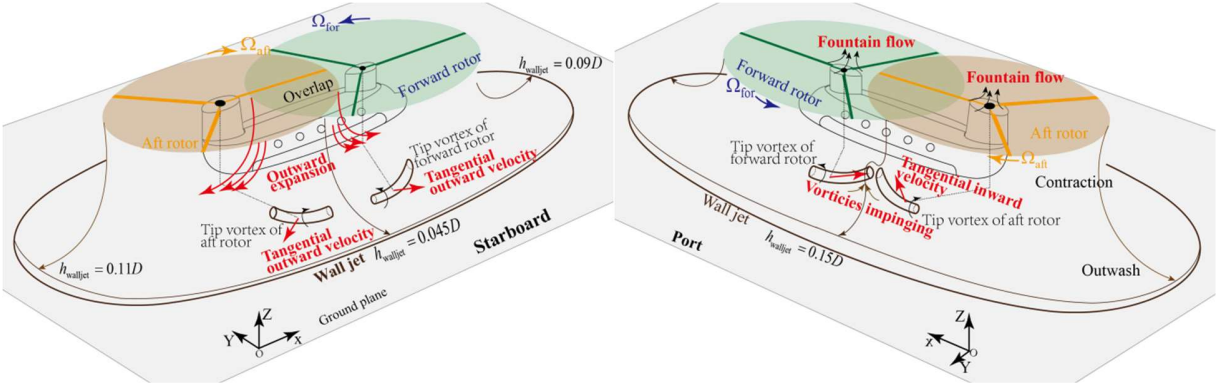

(a) Starboard (b) Port

Fig. 25 Flow complexities of the tandem rotor IGE

Flow visualizations at different sectional planes are shown in Fig. 26. Similar to the single rotor in Fig. 16(b), snapshot of the predicted flow field in Fig. 26(a) shows the characteristic formation of the tip vortices and vortex sheet structures in the wake below the rotor, and the wall jet around the ground plane. Also, the figure reveals the onset of vortex pairing of the older vortices as they approach the ground plane. As expected, the interaction of the forward rotor tip vortices and the inboard sheet with that of the aft rotor results in stronger vorticity distribution and vortex-ground plane interaction in the overlapping area. The flow visualization shown in Fig. 26(b) suggests that the

thickness of the approximated slipstream indicated by the tip vortices on the port side is greater than that of the starboard side as shown in Figs. 22 and 23(b). The reason for the differences can be attributed to the fact that the wake interaction between the forward and aft rotors on the port side is stronger than that of the starboard side. This is also confirmed by the flow visualization at the *yz* sectional plane of both rotors as shown in Figs. 24(c) and (d). In addition, it can be seen that the aft rotor produces a thicker wall jet on the port side compared to the forward rotor. This is a result of the inclination of the forward rotor, which forces the forward tip vortices to penetrate into the outwash of the aft rotor.

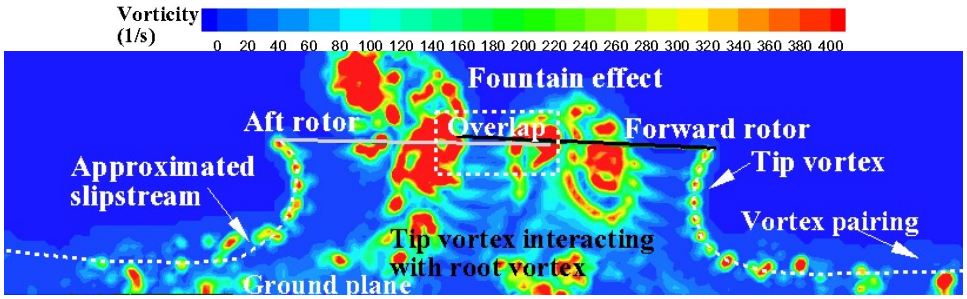

(a) *xz* sectional plane

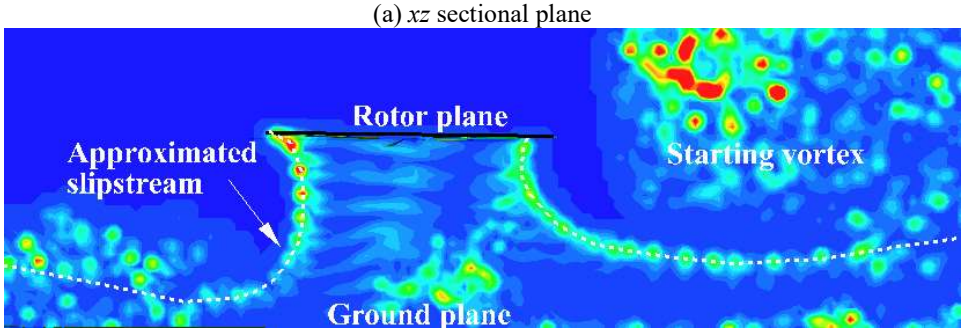

(b) *yz* sectional plane of the aircraft

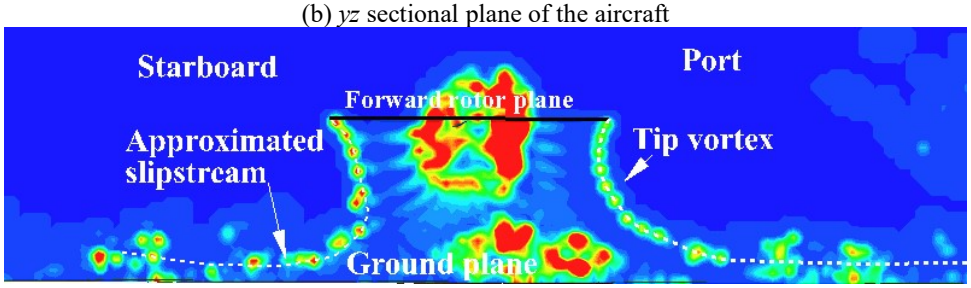

(c) *yz* sectional plane of the forward rotor

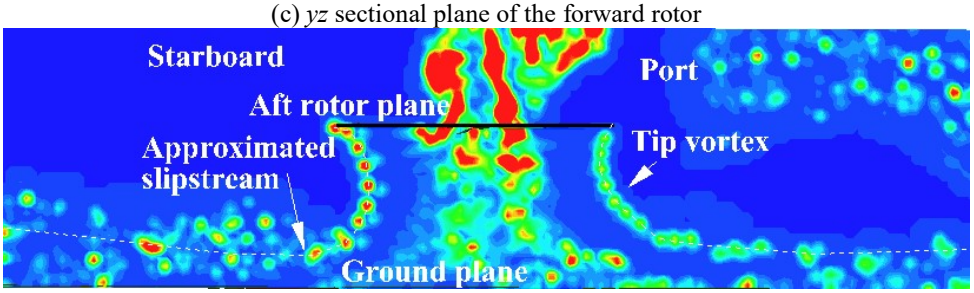

(d) *yz* sectional plane of the aft rotor

Fig. 26 Flow visualization of the tandem rotor IGE (*h*/*R*=1.156)

The flow visualizations of the wake at different distances above the ground in Fig. 27 provide some insight into the characteristics of the wake structure. In Figs. 27 (a-c), even after 30 rotor revolutions the starting vortex is still in the computational domain and close to the tandem rotor on the port side. Conversely, the starting vortex on the starboard side is out of the domain. The reason for the difference can be understood by comparing the variation of the tangential inward velocity on the port and starboard sides (see Fig. 25). The effect of the opposite rotational direction is confirmed in Figs. 27(d) and (e). It can be seen, as expected, that the tip vortices of the forward and aft rotors on the port side impinge on each other with a tangential inward velocity, while those vortices on the starboard side convecting in opposite direction are pushed outward of the tandem rotor. Additionally, it is interesting to note that in Fig. 27 (f), the vortices on the starboard side of the tandem rotor, compared to the port side, expand further outward as they come into proximity of the ground.

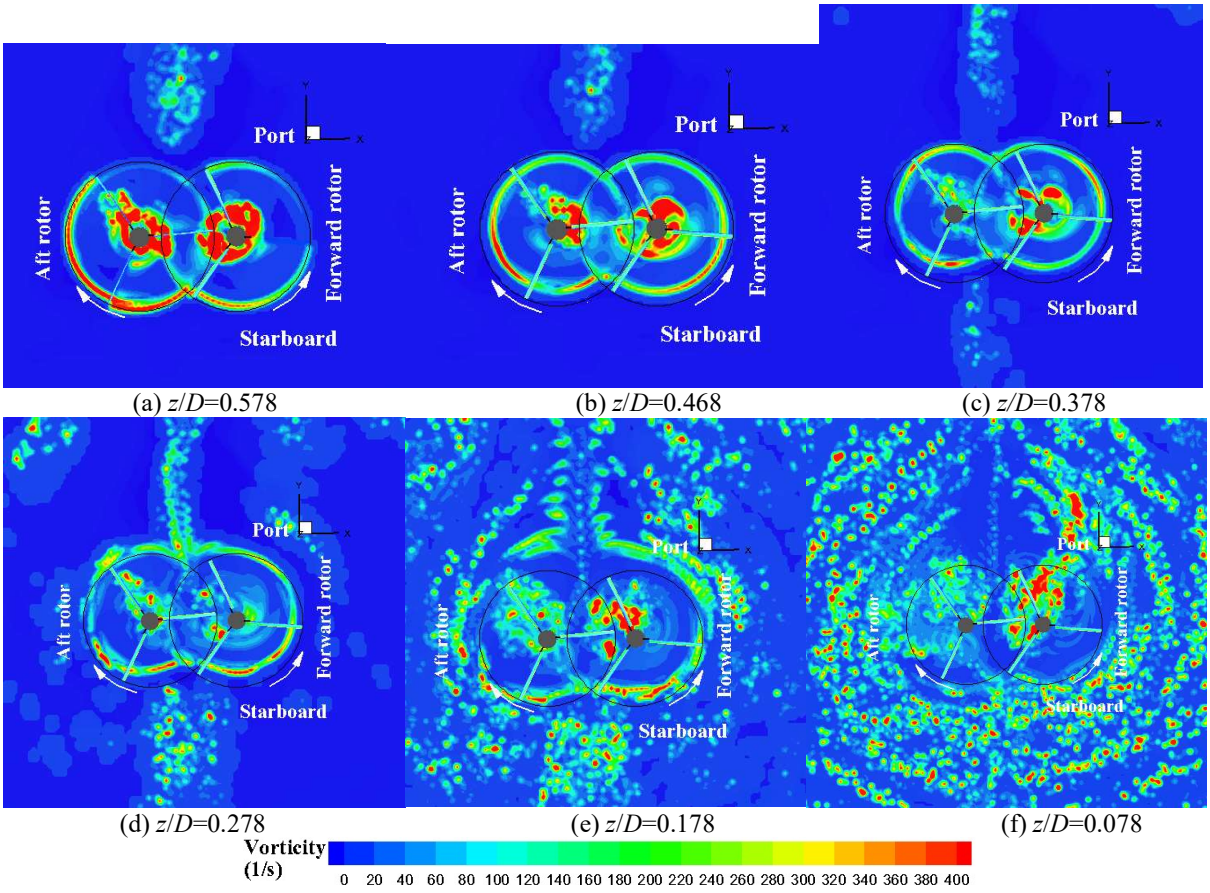

(a) z/D=0.578 (b) z/D=0.468 (c) z/D=0.378

(d) z/D=0.278 (e) z/D=0.178 (f) z/D=0.078

Fig. 27 Flow visualization of the tandem rotor IGE (h/R=1.156) at different distances above the ground

IV.Conclusion

A novel vortex-based approach is established to predict downwash and outwash (DWOW) of an overlapping tandem rotor in ground effect. The aerodynamics of the multi-rotor are modelled using an unsteady panel method, and the unsteady behaviour of the multi-rotor tip vortices and wake are predicted through the viscous vortex particle method. Viscous effects on the ground plane are accounted for by a viscous boundary model through generating a vortex sheet on the ground surface and diffusing the vortex into the flow field.

The present approach is applied to an isolated full-scale Lynx tail rotor and a 172 mm-diameter rotor in ground effect. The results show that the predicted trajectories of the tip vortices and the radial velocity profiles compare favourably with experimental data and published CFD results based on RANS equations. Compared with CFD of the RANS equations, the present approach is more efficient. Moreover, the present method is also employed to the DWOW of a model CH-47D in ground effect. The variations of the downwash and outwash at various heights below the rotor and radial distances from the center correlate well with the measurements for the single aft rotor OGE and IGE. The predicted DWOW of the overlapping tandem rotor IGE also agrees well with the measurements. Therefore, the present approach has the ability to predict the DWOW of the tandem rotor with favorable accuracy and efficiency.

Like the single rotor IGE, the scaled tandem rotor showed similar maximum wake contraction and radial outward expansion, and produced similar distributions of horizontal velocity. Also, fountain flows in both the forward and aft rotors were observed. Contrary to the single rotor, the peak velocity and the corresponding vertical distance of the velocity maximum of the wall jet for the tandem rotor were greater due to the strong wake interaction between the forward and aft rotors. The interaction of the aft rotor tip vortex with the inboard sheet of the forward rotor resulted in a radial outward expansion in the overlapping area; not seen for the single rotor. Additionally, two tip vortices with opposed directions were observed in the overlapping area of the forward and aft rotors. Outside the rotor plane, slightly above the thickness of the wall jet, the radial outwash velocity of the port side was larger than that of the starboard due to the stronger vorticity of old, aged vortices near the ground plane caused by the anti-clockwise rotation of the forward rotor and the clock-wise rotation of the aft rotor. Contrary to the starboard side, the thickness of the wall jet on the port side was larger.

For the tandem rotor, the wall jet of the aft rotor at the *xz* and *yz* sectional planes was thicker than that of the forward rotor. The fountain flow of the aft rotor was strengthened. The tip vortices of the forward and aft rotors on

the port side were pushed toward the center of the tandem rotor with a tangential inward velocity, while that of the starboard side were pushed outward, which resulted in differences of outwash velocity on the port and starboard sides. It also resulted in the port vortex staying closer to the tandem rotor, whereas the one on the starboard side expanded further outward as it approaches the ground surface.

Acknowledgments

This work was supported by the National Natural Science Foundation of China (Grant No. 11502105), and the support of Natural Science Foundation of Jiangsu Province (Grant No. BK20161537) and the Jiangsu Government Scholarship for Overseas Studies were gratefully acknowledged.

References

[1] Milluzzo, J. I., and Leishman, J. G., "Vortical Sheet Behavior in the Wake of a Rotor in Ground Effect," *AIAA Journal*, Vol. 55, No. 1, 2017, pp. 24, 35.
doi: 10.2514/1.J054498

[2] Sugiura, M., Tanabe, Y., Sugawara, H., Matayoshi, N., and Ishii, H., "Numerical Simulations and Measurements of the Helicopter Wake in Ground Effect," *Journal of Aircraft*, Vol. 54, No. 1, 2017, pp. 209, 218.
doi: 10.2514/1.C033665

[3] Tanner, P. E., Overmeyer, A. D., Jenkins, L. N., Yao, C. S., and Bartram, S. M., "Experimental Investigation of Rotorcraft Outwash in Ground Effect," *Presented at the AHS 71st Annual Forum*, AHS, Virginia Beach, Virginia, 2015, pp. 2655-2680.

[4] Wadcock, A. J., Ewing, L. A., Solis, E., Potsdam, M., and Rajagopalan, G., "Rotorcraft Downwash Flow Field Study to Understand the Aerodynamics of Helicopter Brownout," *Proceedings of the American Helicopter Society Southwest Region Technical Specialists Meeting*, AHS, Dallas-FortWorth, TX, 2008.

[5] Lee, T. E., Leishman, J. G., and Ramasamy, M., "Fluid Dynamics of Interacting Blade Tip Vortices with a Ground Plane," *Journal of the American Helicopter Society*, Vol. 55, No. 2, 2010, pp. 22005-1, 22005-16.
doi: 10.4050/JAHS.55.022005

[6] de Andrea, A., "Numerical Analysis of Unsteady Vortical Flows Generated by a Rotorcraft Operating on Ground: a First Assessment of Helicopter Brownout," *Presented at the American Helicopter Society 65th Annual Forum*, AHS, Grapevine, Texas, 2009, pp. 423-446.

[7] Phillips, C., Kim, H. W., and Brown, R. E., "The Flow Physics of Helicopter Brownout," *Presented at the American Helicopter Society 66th Annual Forum*, AHS, Phoenix, AZ, 2010, pp. 1273-1291.

[8] Rauleder, J., and Leishman, J. G., "Flow Environment and Organized Turbulence Structures Near a Plane Below a Rotor," *AIAA Journal*, Vol. 52, No. 1, 2014, pp. 146, 161. https://doi.org/10.2514/1.J052315

[9] Silva, M. J., and Riser, R., "CH-47D Tandem Rotor Outwash Survey," *Presented at the American Helicopter Society 67th Annual Forum*, AHS, Virginia Beach, VA, 2011, pp. 2917-2937.

[10] Ramasamy, M., Potsdam, M., and Yamauchi, G. K., "Measurements to Understand the Flow Mechanisms Contribution to Tandem-rotor Outwash", *Presented at the AHS 71st Annual Forum*, AHS, Virginia Beach, 2015, pp. 612-647.

[11] Ramasamy, M., and Yamauchi, G, K., "Using Model-Scale Tandem-Rotor Measurements in Ground Effect to Understand Full-Scale CH-47D Outwash," *Journal of the American Helicopter Society*, Vol. 62, No. 1, 2017, pp, 012004-1, 012004-14. doi: 10.4050/JAHS.62.012004

[12] Betz, A., "The Ground Effect on Lifting Propellers," NACA TM-836, 1937.

[13] Cheeseman, I. C., and Bennett, W. E., "The Effect of the Ground on a Helicopter Rotor in Forward Flight," ARC R&M 3021, 1955.

[14] Knight, M., and Hefner, R. A., "Analysis of Ground Effect on the Lifting Airscrew," NACA TN-835, 1941.

[15] Rossow, V. J., "Effect of Ground and/or Ceiling Planes on Thrust of Rotors in Hover," NASA TM-86754, 1985.

[16] DuWaldt, F. A., "Wakes of Lifting Propellers (Rotors) in-Ground-Effect," Cornell Aeronautical Laboratory, Report CAL No. BB-1665-S-3, 1966.

[17] George, M., Kisielowski, E., and Douglas, D. S., "Investigation of the Downwash Environment Generated by V/STOL Aircraft Operating in Ground Effect," USAAVLABS Technical Report 68-52, 1968.

[18] Ferguson, S. W., "Rotorwash Analysis Handbook, Volume I Development and Analysis," Federal Aviation Administration, Technical Report DOT/FAA/RD-93/31, 1994.

[19] Preston, J. R., Troutman, S., Keen, E., Silva, M., Whitman, N., Calvert, M., Cardamone, M., Moulton, M., and Ferguson, S. W., "Rotorwash Operational Footprint Modeling," U.S. Army RDECOM Technical Report RDMRAF-14-02, 2014.

[20] Quackenbush, T. R., and Wachspress, D. A., "Enhancements to a New Free Wake Hover Analysis," NASA CR 177523, 1989.

[21] Wachspress, D. A., Whitehouse, G. R., Keller, J.D., and Yu, K., "A High Fidelity Brownout Model for Real-Time Flight Simulations and Tranners," *Presented at the American Helicopter Society 65th Annual Forum*, AHS, Grapevine, TX, 2009, pp. 1281-1304.

[22] Syal, M., and Leishman, J. G., "Modeling of Bombardment Ejections in the Rotorcraft Brownout Problem," *AIAA Journal*, Vol. 51, No. 4, 2013, pp. 849, 866. https://doi.org/10.2514/1.J051761

[23] Govindarajan, B., and Leishman, J. G., "Predictions of Rotor and Rotor/Airframe Configurational Effects on Brownout Dust Clouds", *Journal of Aircraft*, Vol. 53, No. 2, 2016, pp, 545, 560.
https://doi.org/10.2514/1.C033447

[24] Griffiths, D. A., Ananthan, S., and Leishman, J. G., "Predictions of Rotor Performance in Ground Effect Using a Free-Vortex Wake Model," *Journal of the American Helicopter Society*, Vol. 50, No. 4, 2005, pp. 302, 314.
doi: https://doi.org/10.4050/1.3092867

[25] Brown, R., and Whitehouse, G., "Modelling Rotor Wakes in Ground Effect," *Journal of the American Helicopter Society*, Vol. 49, No. 3, 2004, pp. 238, 249.
doi: https://doi.org/10.4050/JAHS.49.238

[26] Phillips, C., and Brown, R. E., "Eulerian Simulation of the Fluid Dynamics of Helicopter Brownout," *Journal of Aircraft*, Vol. 46, No. 4, 2009, pp. 1416, 1429.
doi:10.2514/1.41999

[27] Zhao, J., and He, C., "Physics-Based Modeling of Viscous Ground Effect for Rotorcraft Applications," *Journal of the American Helicopter Society*, Vol. 60, No. 3, 2015, pp, 1, 13.
https://doi.org/10.4050/JAHS.60.032006

[28] Rossinelli, D., Bergdorf, M., Cottet, G-H., and Koumoutsakos, P., "GPU Accelerated Simulations of Bluff Body Flows Using Vortex Particle Methods," *Journal of Computational Physics*, Vol. 229, 2010, pp. 3316, 3333.
doi:10.1016/j.jcp.2010.01.004

[29] Crozon, C., Steijl, R., and Barakos, G. N., "Numerical Study of Helicopter Rotors in a Ship Airwake," *Journal of Aircraft*, Vol. 51, No. 6, 2014, pp. 1813, 1832.
doi:10.2514/1.C032535

[30] Thomas, S., Lakshminarayan, V. K., Kalra, T. S., and Baeder, J. D., "Eulerian-Lagrangian Analysis of Cloud Evolution using CFD Coupled with a Sediment Tracking Algorithm," *Proceedings of the 67th Annual AHS Forum*, AHS,Virginia Beach, VA, 2011, pp. 298-315.

[31] Kalra, T. S., Lakshminarayan, V. K., and Baeder, J. D., "CFD Validation of Micro Hovering Rotor in Ground Effect," *Presented at the 66th Annual Forum and Technology Display of the American Helicopter Society International*, AHS, Phoenix, Arizona, 2010, pp. 523-544.

[32] Lakshminarayan, V. K., Kalra, T. S., and Baeder, J. D., "Detailed Computational Investigation of a Hovering Microscale Rotor in Ground Effect," *AIAA Journal*, Vol. 51, No. 4, 2013, pp. 893, 909.
doi: 10.2514/1.J051789

[33] Tan, J. F., and Wang, H. W., "Simulating Unsteady Aerodynamics of Helicopter Rotor With Panel/Viscous Vortex Particle Method," *Aerospace Science and Technology*, Vol. 30, No. 1, 2013, pp. 255, 268. http://dx.doi.org/10.1016/j.ast.2013.08.010

[34] Lorber, P. F., and Egolf, T. A., "An Unsteady Helicopter Rotor-Fuselage Aerodynamic Interaction Analysis," *Journal of the American Helicopter Society*, Vol. 35, No. 3, 1990, pp. 32, 42.

[35] Degond, P. S., and Gallic, M., "The Weighted Particle Method for Convection-Diffusion Equations. Part 1. the Case of an Isotropic Viscosity," *Math. Comp*, Vol. 53, 1989, pp. 485, 507.

[36] Degond, P. S., and Gallic, M., "The Weighted Particle Method for Convection-Diffusion Equations. Part 2. the Anisotropic Case," *Math. Comp*, Vol. 53, 1989, pp. 509, 525.

[37] Cottet, G. -H., and Koumoutsakos, P., *Vortex Methods, Theory and Practice*, Cambridge University Press, Cambridge, 2000.

[38] Greengard, L., and Rokhlin, V., "A Fast Algorithm for Particle Simulations," *Journal of Computational Physics*, Vol. 135, No. 2, 1997, pp. 280, 292. https://doi.org/10.1016/0021-9991(87)90140-9

[39] Koumoutsakos, P., Leonard, A., and Pepin, F., "Boundary Conditions for Viscous Vortex Method," *Journal of Computational Physics*, Vol. 113, 1994, pp. 52, 61.

[40] Ploumhans, P., Daeninck, G., and Winckelmans, G., "Simulation of Three-dimensional Bluff-body Flows Using the Vortex Particle and Boundary Element Methods," *Flow, Turbulence and Combustion*, Vol. 73, 2004, pp. 117, 131.

[41] Poncet, P., "Topological Aspects of Three-dimensional Wakes Behind Rotary Oscillating Cylinders," *Journal of Fluid Mechanics*, Vol. 517, 2004, pp. 27, 53.

[42] Rosenhead., L., *Laminar Boundary Layers*, Oxford University Press, Oxford, 1963, Part II Introduction Boundary Layer Theory, pp. 46, 109.

[43] Ploumhans, P., and Winckelmans, G. S., "Vortex Methods for High-resolution Simulations of Viscous Flow Past Bluff bodies of General Geometry," *Journal of Computational Physics*, Vol. 165, 2000, pp. 354, 406.

[44] Ploumhans, P., Winckelmans, G. S., Salmon, J. K., Leonard, A., and Warren, M. S., "Vortex Methods for Direct Numerical Simulation of Three-Dimensional Bluff Body Flow: Application to the Sphere at *R*e=300, 500, and 1000," *Journal of Computational Physics*, Vol. 178, 2002, pp. 427, 463.

[45] Zhang, L. J., and Eldredge, J. D., "A Viscous Vortex Particle Method for Deforming Bodies with Application to Biolocomotion," *International Journal for Numerical Methods in Fluid*, Vol. 59, 2009, pp. 1299, 1320. doi: 10.1002/fld.1867

[46] Colagrossi, A., Graziani, G., and Pulvirenti, M., "Particles for Fluids: SPH Versus Vortex Methods," *Mathematics and Mechanics of complex systems*, Vol. 2, No. 1, 2014, pp. 45, 70.

doi: dx.doi.org/10.2140/memocs.2014.2.45

[47] Light, J.S., "Tip Vortex Geometry of a Hovering Helicopter Rotor in Ground Effect," *Journal of the American Helicopter Society*, Vol. 38, No. 2, 1993, pp. 34, 42.

[48] Filippone, A., Bakker, R., Basset, P. M., Rodriguez, B., Green, R., Kutz, B., Bensing, F., and Visingardi, A., "Rotor Wake Modelling in Ground Effect Conditions," *Presented at the 37th European Rotorcraft Forum*, ERF, Vergiate and Gallarate, Italy, 2011, pp, 29-40.